7-11-2013

Long-Distance Flux Mapping Using Low-Cost Collimated Pyranometers

Jeremy Sment

Jeremy Sment

Candidate

Mechanical Engineering

Department

This thesis is approved, and it is acceptable in quality and form for publication:

Approved by the Thesis Committee:

Dr. Andrea Mammoli, Chairperson

Dr. Peter Vorobieff

Dr. Clifford Ho

**LONG-DISTANCE FLUX MAPPING USING
LOW-COST COLLIMATED PYRANOMETERS**

by

JEREMY SMENT

**PREVIOUS DEGREES:
BACHELOR OF SCIENCE IN MECHANICAL ENGINEERING
UNIVERSITY OF NEW MEXICO 2011**

THESIS

**Submitted in Partial Fulfillment of the
Requirements for the Degree of**

Master of Science in Mechanical Engineering

**The University of New Mexico
Albuquerque, New Mexico**

May 2013

ACKNOWLEDGMENTS

Long-Distance Flux Mapping Using Low-Cost Collimated Pyranometers

by

Jeremy Sment

B.S. in Mechanical Engineering, University of New Mexico 2011
M.S. in Mechanical Engineering, University of New Mexico 2013

ABSTRACT

Concentrating solar thermal power tower plants with capacities of 100 MW$_e$ or greater require large heliostat fields with heliostats over 1,500 m (nearly a mile) away from the tower. The accuracy and performance of these heliostats must be evaluated and understood as new heliostat designs emerge to reduce costs. Conventional beam characterization systems that use photographs of the reflected beam on a tower-mounted target are typically not large enough to capture the beam at large distances, and the magnitude of the irradiance for long-distance heliostats is quite low (only a fraction of a sun), which can make the beam image difficult to discern from the ambient lighting on the target.

The Long-Range Heliostat Target (LRHT) is a vertical array of collimated pyranometers deployed to a test site via flat-bed trailer and quickly erected on an aluminum truss tower. Once the sensors have been aimed at the heliostat, the heliostat beam is swept azimuthally across the array whereupon the data is stitched into a flux map

indicating horizontal and vertical beam dimensions and flux intensities. The LRHT was used to evaluate beam shape, peak flux, canting adjustment, and total power of heliostats and single facet reflectors at distances from 300-1700 meters. Results were compared to theoretically rendered flux maps created by computational ray tracing algorithms, and to IR-filtered, visual-band-filtered and non-filtered photographs taken on the beam characterization system (BCS) at the National Solar Thermal Test Facility at Sandia National Laboratories.

Table of Contents

TABLE OF FIGURES

xv

LIST OF TABLES

1. INTRODUCTION

Concentrating solar power (CSP) systems use collectors to focus solar irradiance incident on a large area onto receiver with a much smaller area. This concentrated irradiance can reach temperatures up to and exceeding 4000°C providing enough energy to heat a working fluid sufficiently to produce energy through a Rankine cycle or less commonly a Brayton cycle (Kuntz Falcone 1986). The collectors manifest as mirrors or reflective membrane that are able to track the sun to maintain a reflected beam on the receiver which transfers the energy to a working fluid such as direct steam or to an intermediate heat transfer material such as salt or particles.

There are three orientations for such a system, linear focus, dish, and central receiver. A linear system arranges the collectors into a parabolic whose light is reflected onto a linear receiver tube carrying the working fluid through the focal line. The troughs are arranged north to South and track on a single axis east to West. There are several operational CSP plants in the world. The first commercial solar trough plant (354MW_t) opened in Southern California in 1984 and still operates today (Kuntz Falcone 1986).

Figure 1. Concentrating solar trough system. Copyright and credit: SkyFuel 2009. Used by permission.   Location, Albuquerque, NM (US Department of Energy 2012).

A point-based system arranges the collectors in satellite dish formation and places a Stirling engine at the central focus point that typically has hydrogen or helium gas which is able to turn the pistons to produce electricity directly. On January 31, 2008 Stirling Energy Systems (SES), broke the world record for solar-to-grid system conversion efficiency at 31.25%. (Sandia, Sterling Energy Systems Sets new world record for solar-to-grid conversion efficiency. 2008)

Figure 2. Stirling Energy Systems (SIS) CSP dish technology. Credit: Sandia National Laboratories/Randy Montoya. Copyright: 2008 Used by permission. Location: Albuquerque, NM (US Department of Energy 2012).

A central receiver system uses a large field of collectors mounted on heliostats to focus the light to a central receiver typically located on a large tower in the central and Southern (for Northern hemisphere plants) side of the heliostat field. The heat transfer fluid, typically water for direct steam applications or molten salt for an intermediate agent, is pumped up to the top of the tower where it enters heat exchangers exposed to the reflected irradiance from the field. The fluid then travels to the power block where electricity is produced before completing the power cycle and returning to the receiver for the next cycle.
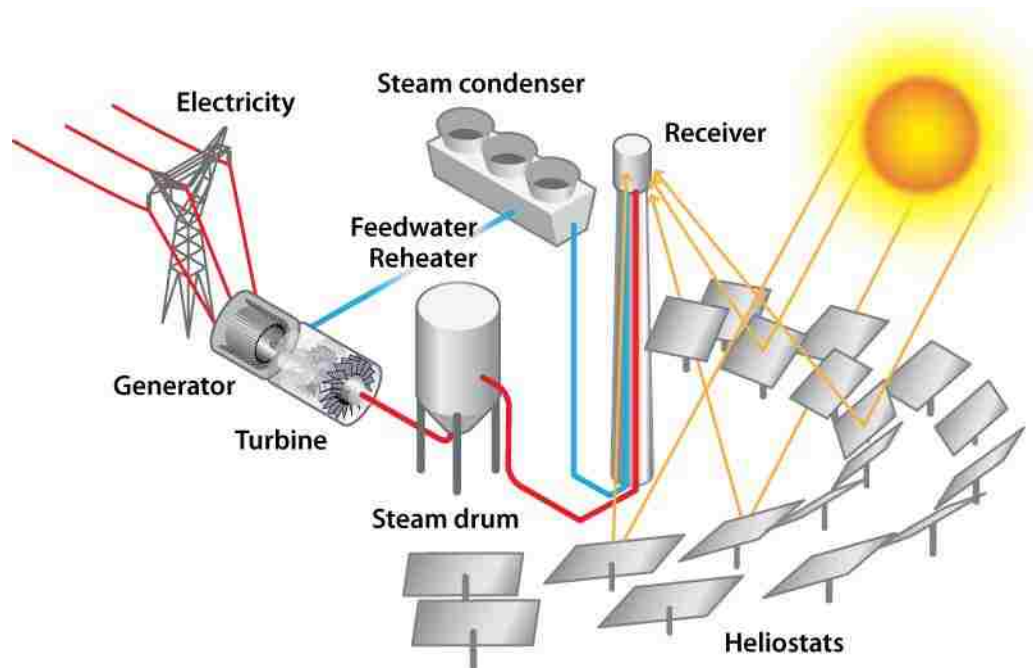
Figure 3. Central receiver concentrating solar power cycle schematic. Copyright/Credit DOE/NREL 1996 (US Department of Energy 2012).

The first documented experiment to utilize this concept occurred in the USSR in the 1950's where large tilting mirrors were mounted to railroad cars to form a crude heliostat. Giovanni Francia constructed the first steam generator to rely on solar energy from 121 small heliostats in 1965. The first system to produce electricity for the grid was a 1 MW solar thermal furnace at Odeillo in the eastern Pyrenees, France. In the United States the U.S. government funded a National Science Foundation research initiative that led to the development of six central receiver type pilot plants worldwide including a $10MW_e$ plant in the Mojave desert east of Barstow that produced steam directly called Solar One, which was rebuilt as the larger molten salt based Solar Two, and the 5 MW_t plant at the National Solar Thermal Test Facility at Sandia National Laboratories (SNL) in Albuquerque, NM (Kuntz Falcone 1986).

4

Figure 4. Solar Two 10 MWe CSP plant with central receiver tower and 1818 heliostats. Copyright 1996: Sandia National Laboratories, used by permission. Location: Barstow, CA. (US Department of Energy 2012)

1.1 **Statement of Problem**

Concentrating solar thermal power tower plants with capacities of 100 MW$_e$ or greater require large heliostat fields, with heliostats over 1,500 m (nearly a mile) away from the tower. For example, *SolarReserve* is presently constructing a 100MWe central receiver type CSP plant in Tonopah, Nevada near Las Vegas with approximately 10,000 116 m^2 heliostats populating a circular field with a maximum radius of approximately 1500 m (Speir 2012).

Figure 5: Solar Tower at Tonopah, Nevada. (source Wikipedia Commons)

The accuracy and performance of these heliostats must be evaluated and understood prior to such a large investment as new heliostat designs emerge to reduce costs. Conventional beam characterization systems (BCS) that use photographs of the reflected beam on a tower-mounted target are typically not large enough to capture the beam at large distances, and the magnitude of the irradiance for long-distance heliostats is quite low (only a fraction of a sun), which can make the beam image difficult to discern from the ambient lighting on the target.
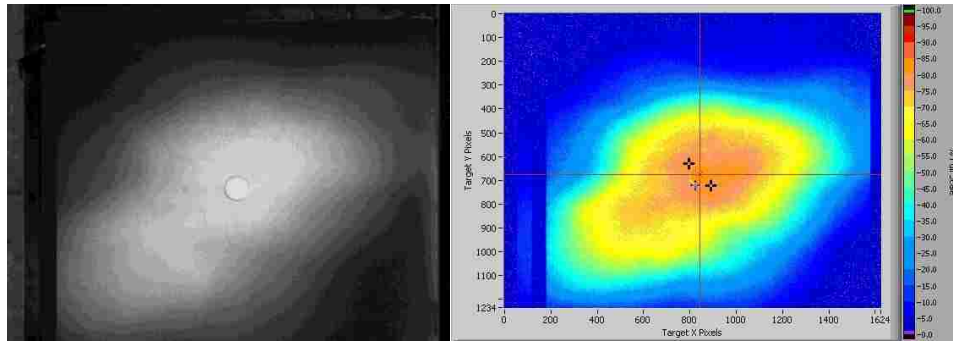
Figure 6: Images from a photograph of a sun beam on tower (left) are converted to a scale based on pixel saturation of the particular camera that was used. These saturation values are then calibrated to show flux distribution within the beam image (right). In long range heliostats the image may be too faint to distinguish from ambient light on the tower.

Furthermore, it is often necessary to test heliostats at multiple distances well before a site is even constructed. This paper presents the design, build and testing of a new portable system that has been developed to more accurately evaluate the flux distribution received from these long-distance heliostats to ensure that they meet requirements for optical accuracy and intensity.

2. APPROACH

The reflected beam from the heliostat is characterized using low cost photodiode-based LI-COR LI-200SA pyranometers that were fitted into PVC collimators. A long-range mobile target was constructed that is comprised of a lightweight telescoping aluminum tower mounted on a flatbed trailer. The collimated pyranometers were mounted in a vertical column over the height of the tower, aimed at the heliostat, and wired to an onboard solar powered data acquisition system. During a test, the heliostat beam is swept horizontally across the column of sensors at an even rate. The values are logged at high frequency yielding an irradiance distribution along discrete vertical transects corresponding to the heights of the sensors. The transects are then plotted on a 3D contour plot and stitched together using interpolation to render the entire irradiance distribution (Sment, Ho, et al., Flux Characterization for Long-Distance Heliostats 2012). See section 4.2.

3. DESIGN OF PROTOTYPE

The primary requirements of the long range target are that it be

1. Capable of measuring direct irradiance normal to the face of the target

2. Tall enough to encompass the span of a heliostat beam at long distances

3. Portable

4. Powered off grid

5. No ground penetration required as dig permits may be difficult to obtain

6. Fast enough response to measure a beam swept across surface

7. High sensitivity to solar flux

8. Able to sustain high wind speeds

3.1 Tower Assembly

Wind impacts on solar equipment in open desert environments cannot be underestimated. An earlier prototype of a long range target was blown over by wind resulting in an extreme safety hazard and large capital loss. Figure 7 shows the first prototype before and after the collapse. Fortunately, no one was near the target when it collapsed and sensors were not yet mounted. For this reason, the redesigned prototype includes a thorough safety analysis of all components and shows that the tower and all of its supporting components including guy wires and fixtures can withstand a 45 m/s (100 mph) wind event.

Figure 7: (Left) First prototype of long distance target erected on trailer. (Right) Wind-blown target has flipped trailer causing significant risk to safety and capital loss.

The test apparatus will consist of a 15.5 m (51 ft) tall two-tier triangular truss frame aluminum T-50XHD tower manufactured by Aluma Tower Inc. The tower will be bolted to a 0.635 cm thick steel base plate that has been welded onto the steel I-beams of a 12.2 m (40 ft) long trailer. LI-COR LI-200 pyranometers encased in PVC pipe housing assemblies will be attached to the tower with aluminum clamps and evenly spaced at 45 cm. The tower will be supported by six pre-tensioned steel guy wires attached at one end to the designated mounting points on the tower, and at the other to one of three concrete blocks. The trailer will be stabilized by four 6.9 m outriggers attached to a junction that has been welded to the trailer. When in position, the trailer is supported by the outriggers and drop-leg trailer jacks with the wheels lifted off the ground.
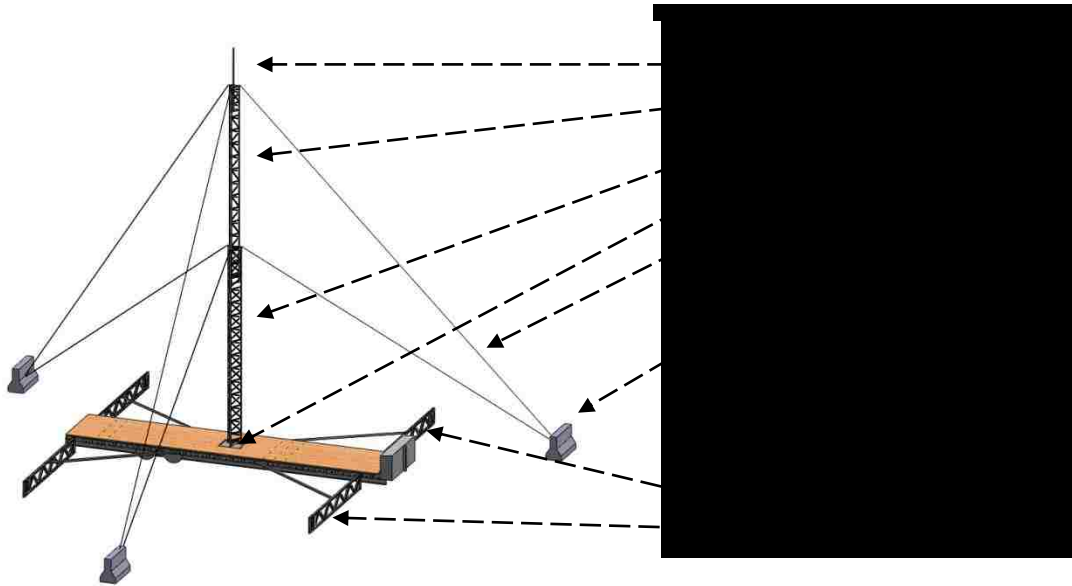
Figure 8: Portable long-range target assembly

3.1.1 Tower

A beam image at solar noon is approximately half the solar cone angle (about 9 mrad) multiplied by the distance to the target plus the area of the reflector. If a 5x5 meter heliostat is located 1600 m (1 mile) away from the target the expected image is 12.4 m assuming no slope error. The design can be scaled to accommodate larger heliostats. The T-50XHD extra heavy duty aluminum tower is made entirely of 6061 T6 aluminum. The tower is bolted to a base plate with five 0.95 cm (3/8 in) bolts which are too small to support the structure without guy wires.

The tower is rated for a max wind speed of 67 m/s (150 mph). Winds above 45 m/s (100 mph) are not expected to occur at Sandia. The ASCE 7-05 "Minimum Design Loads for Buildings and Other Structures" uses a "Basic Wind Speed" which is the 3 second gust speed at 10 m above the ground for analysis of structures. The basic wind speed value for Albuquerque is 40.2 m/s (90 mph) and there are no amplifying factors at

11

the solar facility as it has open plains surrounding the areas where the target will be used. Furthermore, Aluma states a maximum wind speed of 31-34 m/s (70-75 mph) for a tower loaded with 1 m^2 (12 square feet) of equipment. With 30 sensors, the total sensor area sums to 0.6 m^2 (6.6 square feet). (Kidd 2011)

The tower is rated for a max dead weight load of 91 kg (200 lb) (in excess of the guy wire tension and the tower's own weight). Each sensor including the housing and the fixtures to the tower weigh 0.6 kg (1.33 lb) for a total expected weight of approximately 23 kg (50 lb).

The tower's fundamental modal frequency as provided by Aluma is 6.5 Hz. (Kidd 2011) Previous wind data collected during a separate experiment would indicate that gust frequencies are much lower (on the order of 1-1.5 Hz). (Peterka J.A. 1992) However, conclusive data on gust frequencies is currently unavailable so the possibility of a periodic wind event at 6.5 Hz has not been ruled out.

3.2 Superterranean Anchors

The guy wires would ordinarily employ subterranean ground anchors to fix the ends. Many CSP installations are located on Federal, military, or environmentally sensitive lands which may require dig permits for ground penetration over one foot. Much of the open land surrounding the NSTTF is under various jurisdictions making the process of obtaining a separate dig permit for each of several perpetual locations an endless process. In order to make the target more portable it had to be able to operate without such permits. As such a superterranean anchor must be shown to have the equivalent strength of subterranean ground anchors.

Several large concrete blocks were available at no cost. While the weight of these blocks was intuitively sufficient, the blocks needed to be examined for a safe and strong point of attachment to the guy wires, structural constitution and damage, safe transportability with available forklifts, and verification that they would not tip or slide. Figure 9 shows the manufacturer's specifications on their recommended subterranean ground anchor. Figure 10 shows the alternative superterranean ground anchor. The concrete forms weigh approximately 2400 kg (5300 lb).
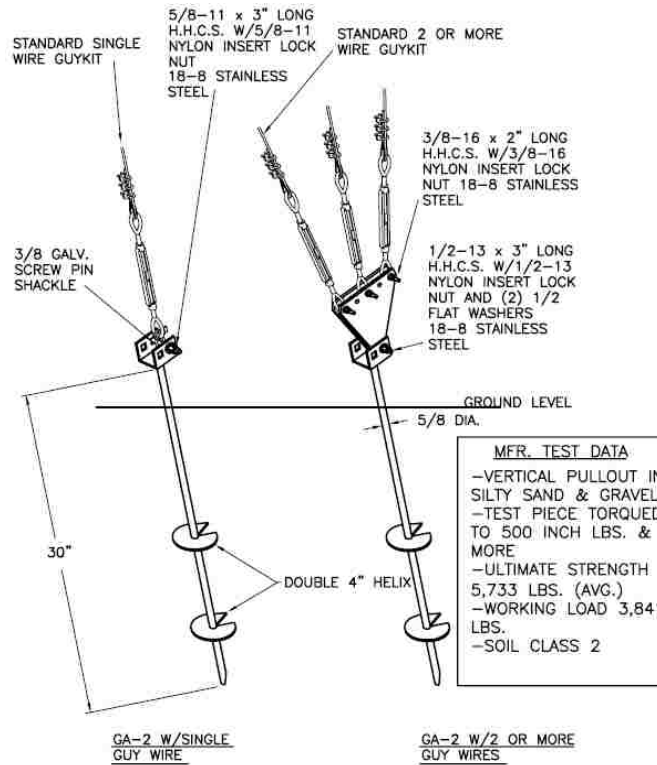
Figure 9: Manufacturer recommended subterranean anchor. (Aluma Tower Company, Inc 1997)

13

Figure 10: 2400 kg concrete anchors 61x91x1.5 cm (2x5x3 ft) were available at no cost. Analysis was performed to show functional equivalence to ground anchors and safety of handling.

The concrete anchors are deduced to have been made with high strength concrete and standard steel reinforcement bar known to greatly improve the performance of concrete forms in tension.

To aid in safe transport and positioning, the concrete blocks had lifting pins embedded in the concrete (Figure 11). An anchor bracket was fabricated to attach the guy wire shackle to the concrete block. The anchor bracket is welded to one of the lifting pins. Finite element analysis was performed on the anchor bracket using SolidWorks' FFE plus proprietary solver. Average element size was .1055 +/- .005276 inches with 81,475 nodes and 54,148 elements.

Figure 11: Rebar reinforced concrete form with lifting pin. Photo provided by a lifting pin system retailer Patterson-online.com is not necessarily the rebar structure in the anchors, but represents an assumed likely interior. (Lifting Pin Anchor System 2011)

Figure 12: Anchor bracket welded to lifting pin. Contact point between bracket and concrete is made to mitigate bending stress on the lifting pin.

Figure 13 illustrates how fixed constraints were applied to the faces surrounding and welded to the lifting pin. A sliding surface constraint was applied to the contact point of the anchor bracket and the concrete. Forces were applied to the face of the bracket holes where the shackle would act. The magnitudes of the forces correspond to the x and y components of the tension in the guy wires calculated in section 3.4.

The results of the analysis show that the anchor bracket in the intended orientation has a static factor of safety of 8.7 (Figure 13). Fatigue analysis at 10^6 cycles reveals a load factor of 1.8. The load factor represents the multiplier of the forces that could survive 10^6 cycles. The anchor bracket could also survive opposite orientation (180˚) with a static factor of safety of 5.5. In general, the anchor bracket will not fail from static loads or fatigue if placed within 30° of the proper orientation shown in Figure 12.
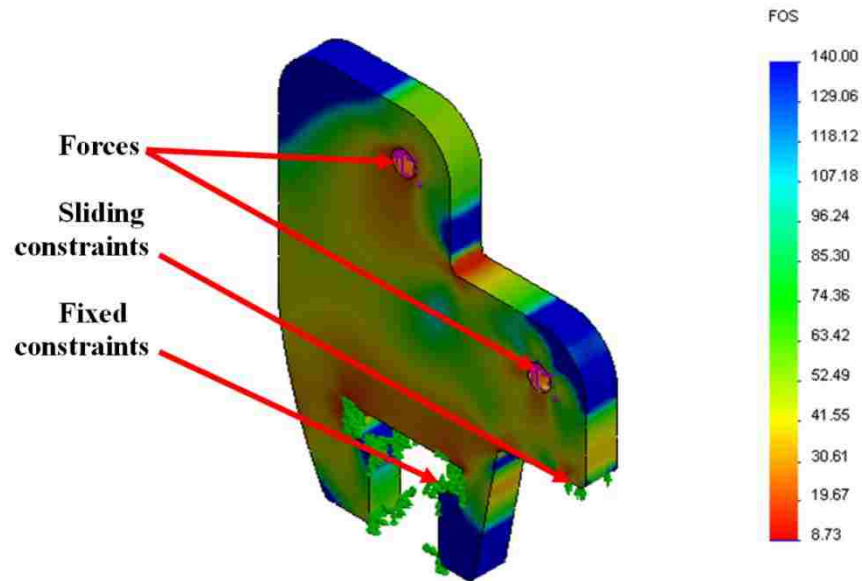
Figure 13: Static factor of safety analysis of anchor bracket. Min FOS = 8.7

16

3.3 Trailer

Tipping analysis had to be performed to show that the new design would not tip during a wind event and additionally that the trailer can handle the heavy blocks that it must transport. The tower is bolted to a steel base plate welded to a 12 m (40 ft) flat-deck trailer. This has a gross vehicular weight rating of 10,160 kg (22,400 lb), and a gross axle weight rating of 4536 kg (10,000 lb). With two axles, the trailer easily handles the weight of the three blocks. The drop leg jacks are also rated for 4536 kg. The baseplate of the tower is a sheet of 6 mm (1/4 in) steel welded directly to the I-beams of the trailer.

The trailer is additionally supported against tipping by 6.9 m (22.5 ft) steel outriggers (Figure 14) which will attach to mounts welded to the trailer (Figure 14). The outriggers will have main members of 10.16 cm (4 in) square steel pipe and inner truss members of 6.3 cm (2.5 in) square pipe. There are diagonal supports of 6.3 cm square pipe.
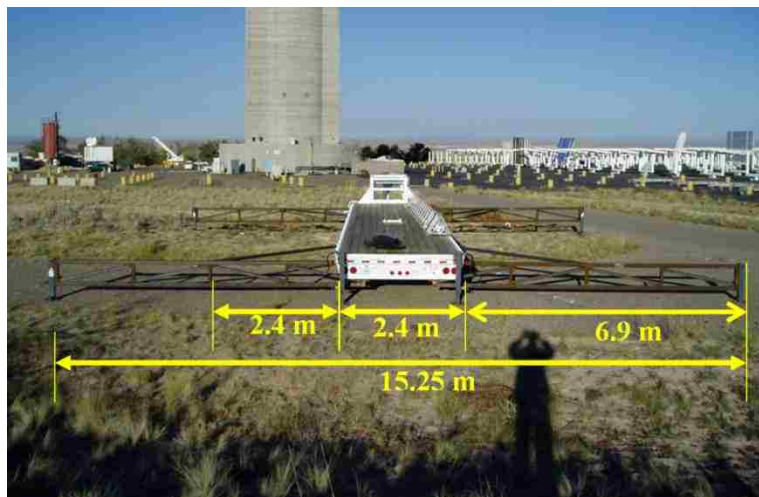
Figure 14: Trailer with outriggers. NSTTF central receiver tower shown in background.

3.4 Wind Force Calculations

Three models were used to predict the wind loading on the tower: (1) TIA-22-G which is the standard used by the manufacturer, (2) the simplified drag force equation, $\left(\frac{1}{2}C_d\rho U^2\right)$ and (3) CFD analysis using SolidWorks Flow Simulation. (See APPENDIX B. CFD Pressure analysis, APPENDIX C. Simplified Drag Force, and APPENDIX D. TIA-22-G Standard) The largest wind forces found via the simplified drag force formulas were used as the basis for the strength/weight requirements of the components as safety was the highest priority under these particular circumstances. The guy wire tension resulting from the wind loading on the truss tower was then applied to the concrete block to determine first, what weight was necessary to provide enough static friction to not slide on loose sand, and second, to determine what dimensions the block would need to have in order to avoid tipping.

The wind velocity is modeled at 45 m/s (100 mph), parallel to the ground along a single guy wire (normal to the tip of the triangular frame) in such a manner to make all wind forces apply only to a single anchor. It can be shown through a force balance using guy wire tension forces against friction forces on the anchor that using a 5500lb block of concrete is more than adequate to support the tower under a 44 m/s (100 mph) wind load. Calculations are shown in appendices for area, wind force, guy wire tension, friction, and tipping moment. (See APPENDIX A. Wind Surface Area Calculations, APPENDIX E. Guy Wire Tension CALCULATIONS, APPENDIX F. Concrete Anchor Forces, and APPENDIX G. Trailer Moments.)

Table 1: Total wind forces on tower during a 45 m/s (100 mph) wind event calculated using three different methods

Wind Load Model	*Wind Force at 45 m/s (100 mph)*
TIA-22-G	2.6 kN (599 lbf)
Simplified	5.7 kN (1281 lbf)
CFD	3.0 kN (1127 lbf)

Using most conservative analysis parameters from the simplified wind force model, the proposed use of the tower is well within the limits provided by the manufacturer. The tower is rated for a max wind speed of 67 m/s (150 mph), while the basic wind speed for Albuquerque is 40.2 m/s (90 mph). The minimum weight of anchor needed to avoid translation is 2000 kg (4411 lb), while the anchors are 2495 kg (5500 lb). The minimum base width of anchor to avoid tipping is 0.396 m (1.3 ft), while the concrete anchors have a minimum base of 0.61 m (2 ft). The moment resisting tipping of the trailer in 45 m/s (100 mph) wind is 1829 N-m (1349 lb-ft), in the event that this tipping moment is exceeded, the outriggers can resist the remaining moment with approximately a 22:3 outrigger-length-to-trailer-height advantage.

Table 2: Summary of Force/Moment Calculations during a 45 m/s (100 mph) wind event and Factor of Safety (FOS).

Member	Applied Force/Moment	Ultimate Force/Moment	FOS
Upper Turnbuckle*	1468 N (330 lb)	5300 N (1200 lb)	3.6
Lower Turnbuckle*	4426 N (995 lb)	5300 N (1200 lb)	1.2
Block Force	5204 N (1170 lb)	6588 (1481 lb)	1.3
Block Moment	3173 N-m (2340 lb-ft)	8620 N-m (6358 lb-ft)	2.7
Trailer Moment	1525 N-m (1125 lb-ft)	3356 N-m (2475 lb-ft)	2.2
* Turnbuckle is weakest member in the guy wire assembly.			

3.5 Collimated Pyranometers

The collimation process makes pyranometers respond like pyrheliometers by only allowing light at less than a 5° angle-of-incidence to reach the sensor. In this configuration the LI-COR flux reading agrees with the Eppley normal incidence pyrheliometer (NIP) within 0.5%, but costs approximately 90% less and has a much faster response time. (King, Boyson and Bower, Improved Accuracy for Low-Cost Solar Irradiance Sensors 1998) The cost of a LI-COR 200SL50 is approximately $300. A pyrheliometer can cost approximately $3000. The collimation process requires inexpensive PVC tubing and labor costs for assembly. A plastic collimator tube is painted black on the inside and fitted with baffles such that it has the same acceptance range as a thermopile pyrheliometer. The tube is placed over the pyranometer and a low-cost clear plastic lens was used to seal the column at the opposite end. (King, Boyson

and Bower, Improved Accuracy for Low-Cost Solar Irradiance Sensors 1998) Optical information is not available on the clear plastic lens. Furthermore, the plastic was not UV resistant. Twenty-seven to thirty collimated pyranometers are mounted in a vertical column over the height of the tower, aimed at the heliostat, and wired to an onboard data acquisition system housed in a weather proof enclosure (Figure 15). The data acquisition computer is powered off-grid by a 225 W solar panel and 24V battery assembly.

Figure 15: Left: Collimated LI-COR pryanometer. Middle: Photo of trailer-mounted mobile heliostat target with NSTTF central receiver tower in background. Right: close-up of collimated pyranometers mounted on aluminum tower.

3.5.1 *Pyranometer Response*

LI-200 pyranometers have a linear response range up to 3000 W/m^2 which is adequate for long distance heliostats but often too low to characterize heliostats at close range. Furthermore these pyranometers may warp if the temperature exceeds 80° C. The resolution is approximately 0.1 W/m^2. LI-200 have a bias error of 1% up to 3000 W/m^2 and a random error up to 5% and a stability error less than 2% per 1 year period. (LI-COR Biosciences 2005) The sensors used in this paper are less than 2 years old.

The LRHT requires a fast response time from the sensors. A complete beam sweep typically takes less than three seconds. The LI-COR LI-200 has a response time of 10μs while the Eppley NIP has a 1 second response time. Both devices were mounted and pointed at a heliostat beam while voltage was logged at 100 Hz in order to characterize the data from each type of sensor (Figure 16). Figure 17 shows that the LI-COR was able to reach its final voltage sooner than the NIP. Unlike the NIP, the LI-COR is sensitive to the periodic tracker adjustments which can be observed as little spikes in Figure 17 occurring every 10 seconds.

Figure 16: Eppley NIP (left) and Collimated LI-COR LI-200 (right) are aimed at a heliostat to test for response time. (Fisher 2010)
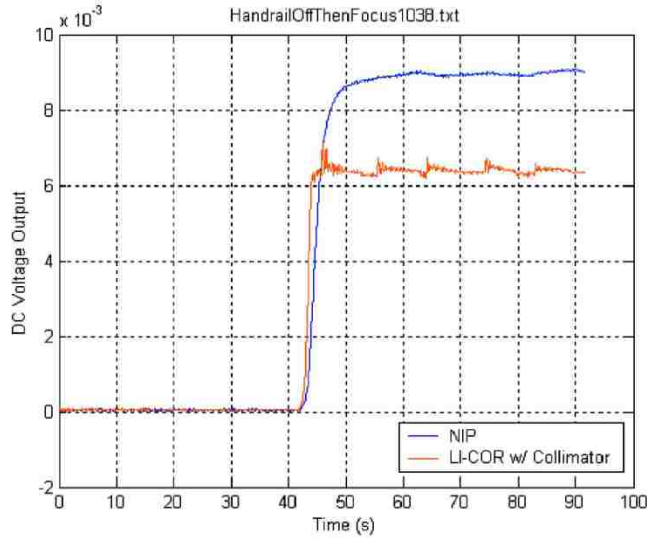
Figure 17: Voltage response of LI-COR and NIP. (Figure provided courtesy of Dan Fisher) (Fisher 2010)

3.5.2 Pyranometer Calibration

The pyranometers were calibrated using a technique pioneered by David King et al that uses a fourth order polynomial fit to flatten the spectral response of the LI-200 so that it behaves more like a broadband pyrheliometer across its spectral range. (See eqn. 3.1) (King, Boyson and Bower, Improved Accuracy for Low-Cost Solar Irradiance Sensors 1998). The function also accommodates for the effects of temperature and angle of incidence on the LI-200's response.

expression to correct measured response R for AOI, solar spectrum and temperature.

$$E_t = \frac{R \cdot E \cdot [1 - \alpha(T - T_0)]}{C_n \cdot f_1(AM_a) \cdot f_2(AOI)}$$

(3.1.)

Where:

23

C_n = Calibration number for device, (mV)
α = temperature coefficient, (1/°C)
T = device Temperature, (°C)
T_o = reference Temperature, (25 °C)
f_1 (AM$_a$) = dimensionless polynomial
f_2 (AOI) = dimensionless polynomial

Figure 18 shows the standard spectral response of the LI-200SA (in green) along with the extraterrestrial and sea-level irradiance at AM1.5 curves. Figure 19 shows that the calibrated spectral irradiance curves exhibit a sharper rise, a flattened response, and are skewed to peak near 500 nm wavelength as does the solar irradiance at AM1.5. The irradiance is a function of the measured pyranometer response, temperature, and a dimensionless polynomial function of air mass. The coefficients to the polynomial were adopted from King's paper. (King, Boyson and Bower, Improved Accuracy for Low-Cost Solar Irradiance Sensors 1998) Future research is needed to validate the adoption of the coefficients in this application.
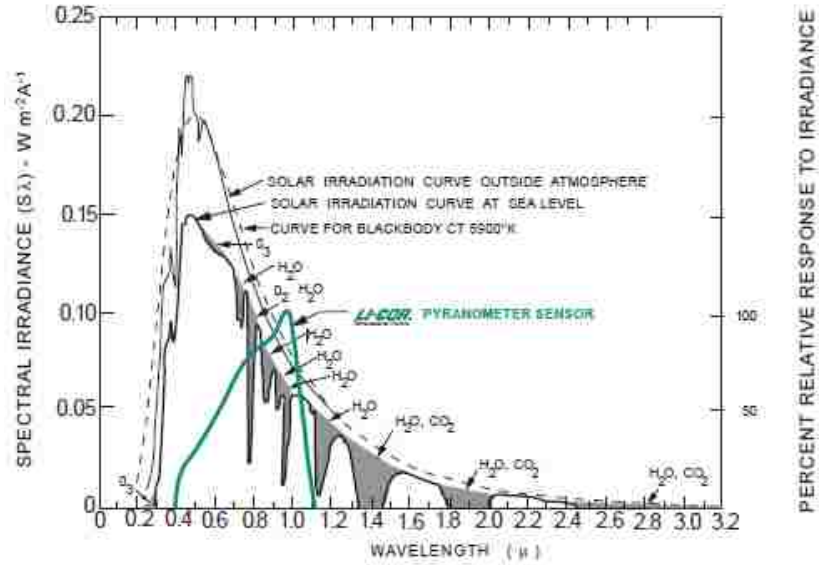
Figure 18: The LI-200SA pyranometer spectral response is overlaid with the extraterrestrial solar irradiance and the solar irradiance at Air Mass = 1.5 (Copyright Licor Inc. Used by Permission) (LI-COR Biosciences n.d.)
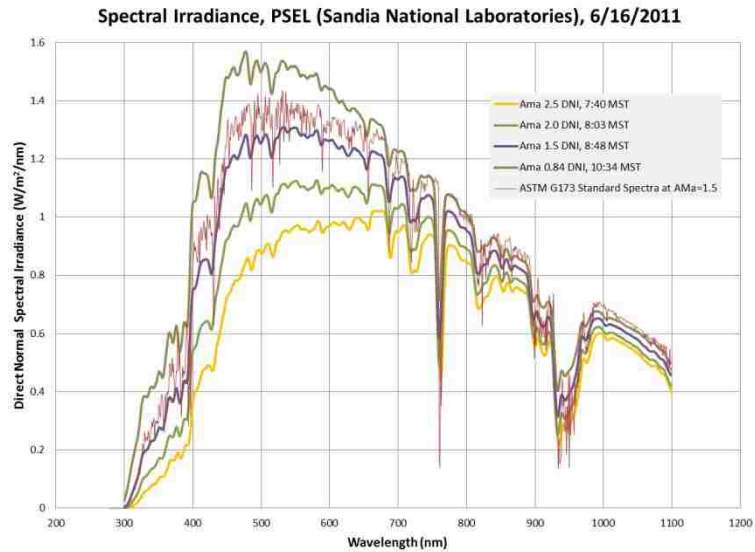
Figure 19: Spectral Irradiance curves of calibrated LI-COR LI-200 pyranometers based on data measured at different air mass, and the ASTM G173 standard spectra at AM_a=1.5. Data taken at Photovoltaic Systems Evaluation Laboratory (PSEL) by Jay Kratochvil. Used by permission.

During the calibration process the collimated pyranometer and an Eppley pyrheliometer were pointed directly at the sun. For each sensor, data were logged continuously from one hour before air mass 1.5 to one hour after. A calibration constant (C_n) was then calculated to fit the pyranometer response to the pyrheliometer under specific conditions. More research is required to determine whether these calibration constants are stable or consistent throughout the year. There have been incidents where the calibration constant for a given sensor was incorrect and the sensor had to be replaced. Figure 20 shows a problematic image on the left where a batch of incorrectly calibrated sensors was used. The image on the right has been smoothed by swapping out sensors and re-aiming others.
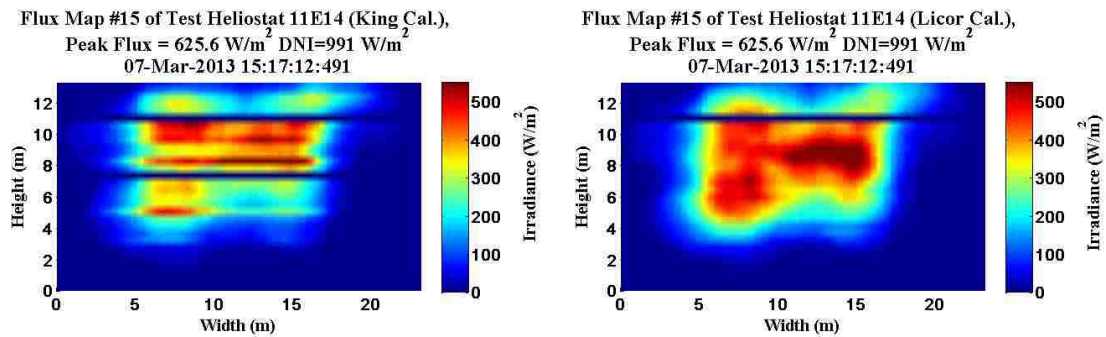
Figure 20: Dubious calibration constants can cause deformed flux maps (left). Swapping sensors, recalibrating, and re-aiming sensors can improve results (right).

4. OPERATIONAL PROCEDURE

Once the tower has been erected, the sensors must be mounted at even intervals over the height of the tower. Each sensor must be aimed directly at the heliostat so that the maximum irradiance is able to reach the sensors. Once the sensors are aimed, the beam can be swept horizontally across the vertical array to create a flux map.

4.1 Set-up

The collimated pyranometers are mounted in an aiming assembly made of hardware that allows rotation about horizontal and vertical axes. While the heliostat beam is set to track on the center of the target, each sensor must be hand aimed by a technician. Unmanned aiming designs are discussed in the future research section below.

An aiming tool which accompanies the technician on a boom lift creates a beeping sound while the sensor is reading a value within 1% of the maximum irradiance that particular sensor has registered during the aiming process. The beeping sound is convenient as glare may inhibit monitor visibility. The technician then sweeps the sensor across the incident beam horizontally until the beeping stops. The sensor is then slowly returned until the beeping returns at which point the sensor is in its optimal horizontal location. The process is then repeated with vertical rotations. Each sensor takes less than five minutes to point so light variation due to solar position is not ordinarily a significant factor. When solar variation is a factor and the sensor cannot reach its prior peak value, numeric indicators can inform the technician of the intensity level to ensure that each sensor is peaking at a similar level and whether a global irradiance shift is affecting the reading. The number of sensors on the tower is a tradeoff between the required level of

resolution and material and labor costs. The test performed below used a 45 cm (18 inch) spacing accommodating 30 sensors.

Figure 21: Author aims sensor at a light source. (Sment, Ho, et al., Flux Characterization for Long-Distance Heliostats 2012). At sufficient distance the heliostat beam is not dangerous.

4.2 Data Analysis

Calibrated data from the LRHT is rendered as a contour plot. The horizontal x-axis represents the beam width and is the product of sweep rate, distance, and time. Sweep rate is a function of the mechanical sweep rate of the heliostat's azimuth drive, and the sun's position. The mechanical sweep rate in rad/sec is multiplied by two to account for the half-angle effect, which causes the beam to move at twice the angular velocity of the reflector. The horizontal component of the angular velocity must then be extracted by multiplying the nominal beam sweep rate by cosine of the apparent solar elevation half-angle. The sweep time of each sample is calculated as the sample index divided by the sampling rate of the data acquisition system. The physical heights of the sensors in meters constitute the vertical y-axis. Linear interpolation is used to provide an equal number of data points in the x and y directions to create a mesh upon which irradiance data can be plotted.

28

5. PROTOTYPE EVALUATION

5.1 Evaluation Procedure

The accuracy of LRHT flux maps was evaluated on three criteria: detection of peak flux, beam shape and size, and flux distribution within beam. The peak flux was compared to results from a commercial ray tracing software that renders an ideal image as it would appear at the location of the target as a function of solar position, reflector location, and user specified optical parameters of the reflector configuration. The beam shape and size was quantified by locating the centroid of the beam image and calculating the height and width dimensions containing 95% of the power.

The beam dimensions containing 95% of the power were based on the distance from the centroid. The centroid's x coordinate was determined by multiplying each power value by the distance from the origin, summing all these moments, and dividing by the total power value. The percentage of power contained in each row across all columns was calculated and added to the adjacent row moving from the centroid outward to the edges such that approximately 50% of the power is to the left of the centroid and 50% is to the right. The beam width is then specified as the difference between the width measurements corresponding to 47.5% of the power on either side of the centroid. The process was repeated in the y dimension to specify the beam height.

In addition to the ideal image modeled using ray tracing, the LRHT flux maps were qualitatively compared to images taken on the central receiver tower located 160 m west and inspected for resolution of anomalies and idiosyncrasies associated with actual heliostat imperfections. The flux maps were also compared to values computed using the

traditional beam characterization system (BCS) which uses a digital camera whose pixel saturation values in a photograph of the beam image as reflected on the white surface of the central receiver tower are converted to flux values through a calibration process.

5.2 **Evaluation Results**

5.2.1 Peak Flux and Dimensions

On January 5, 2012 at solar noon, the test heliostat was swept across the LRHT. Figure 22 shows a theoretical irradiance distribution on the LRHT from the test heliostat calculated using ray tracing. While the precise reflectivity and slope error of the test heliostat is not known, a reflectivity of 0.85 and RMS slope error of 1 mrad was chosen as a best estimate. Figure 23 shows the measured irradiance distribution as rendered by the LRHT at the same time and date.
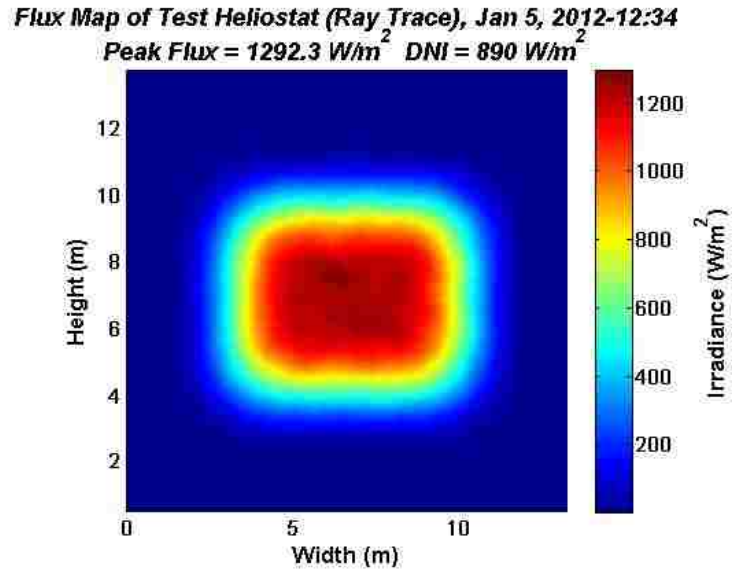
Figure 22: Simulated irradiance distribution on the long-range heliostat target on January 5, 2012 at 12:34 pm. reflectivity=.85, slope error = 1 mrad, DNI=890, Focal length=1500m, peak flux = 1292 W/m2. (Sment, Ho, et al., Flux Characterization for Long-Distance Heliostats 2012)
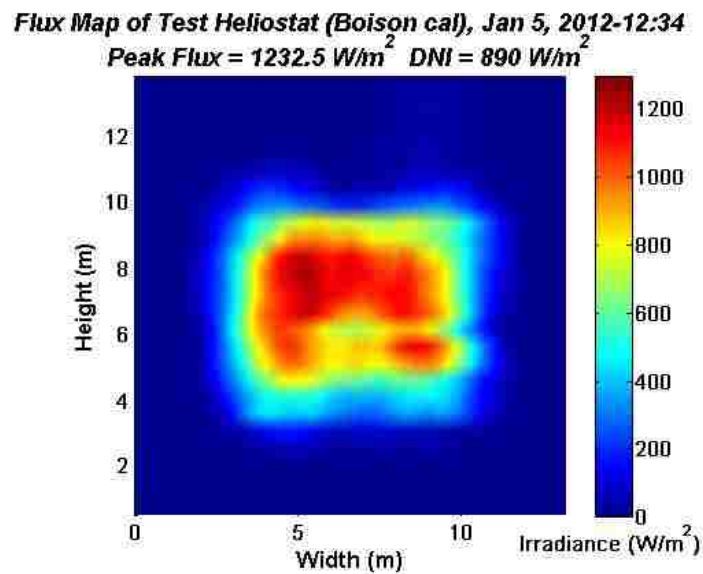
Figure 23: Flux map of test heliostat beam as rendered by LRHT on January 5, 2012 at 12:34 pm. DNI=890, peak flux = 1233 W/m2. (Sment, Ho, et al., Flux Characterization for Long-Distance Heliostats 2012)

The overall size and shape of the theoretical and empirical images have many similarities. The peak flux, total power, and beam dimensions containing 95% of the total power of the beam image were compared for validation. Table 3 summarizes the differences between the two methods of beam characterization. The peak flux measurements show agreement between the two methods within the 11% margin of uncertainty (see 3.5.2). The theoretical peak flux under the specified conditions was 1292 W/m^2 while the measured peak flux was 1233 W/m^2. Power was estimated by multiplying the measured flux value by the area contained in the sample which is the difference in sensor heights multiplied by the x-distance per sample. Total power of the LRHT image is presumed to be the sum of all power calculations over all cells.

Table 3: Peak Flux, and beam shape data as rendered by the Ray Trace method, and the Long Range Heliostat Target.
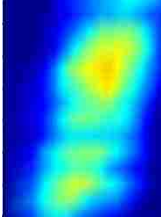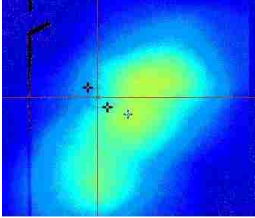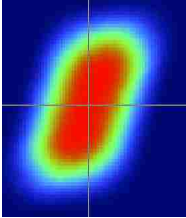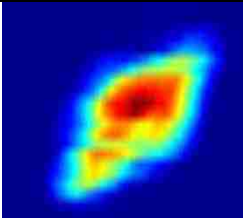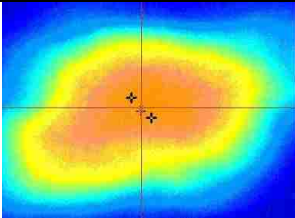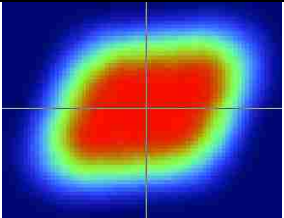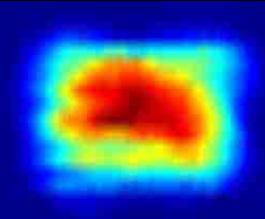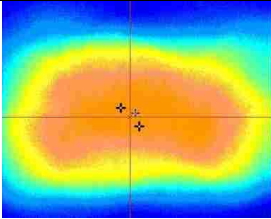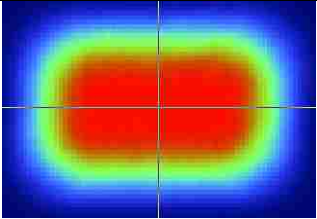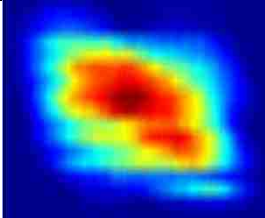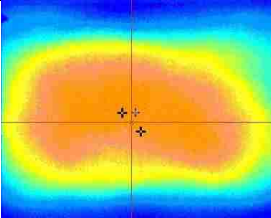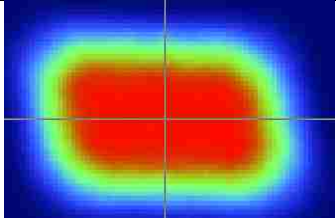
	Ray Trace	*LRHT*	*Median Error*
Peak Flux	1,292 W/m^2	1,233 W/m^2	.05
Total Power	46326 W	41204 W	.11
95% Beam Width	7 m	7.9 m	.14
95% Beam Height	5.9 m	4.8 m	.19

5.2.2 Qualitative Features and Power

Tests were taken throughout the day on July 19 to assess the LRHT's qualitative ability to render the changing beam shape over the day. The beam characterization system (BCS) procedure takes digital photographs of the central receiver tower wall with and without a beam. The pixel saturation values of the tower wall without the beam are subtracted from the saturation values with a beam. Camera specific constants are then

used to convert pixel saturation to flux values. The images in Table 4 show good agreement with the BCS images taken on the central receiver tower located 160 m due west of and about 60 m above the LRHT and the ray trace model of the beam at the LRHT location. While it is expected that the beam shape will differ in separate locations there are some details that can be identified in both. At 8:00 am the LRHT and the BCS images both represent two hot spots within the beam shape. The slope is in the same direction throughout the day. As expected, the LRHT image is narrower due to it being more normal to the test heliostat. At solar noon, the remote target correctly rendered some detailed anomalies such as the horseshoe shape.

Table 4: Qualitative comparison of beam shape as rendered by three methods at different times of day. (Sment, Ho, et al., Flux Characterization for Long-Distance Heliostats 2012)

	LRHT	BCS Image on Central Receiver Tower	Ray Trace
8am			
11am			
1pm (Solar Noon)			
2pm			

The image taken at solar noon has been singled out for more quantitative validation in Figure 24 and Figure 25. The peak flux value of ~1325W/m^2 is near the predicted value. The estimated total power is close to the theoretical value based on the specified reflectivity. There is more significant error in the height dimension. There is an indication in the image that 95% of the power may be distributed across a narrower

height band than is predicted by ray tracing. The results from the three methods are summarized in Table 5.

Table 5: Peak Flux, total power, and beam dimensions containing 95% of total power as rendered by the Ray Trace method, and the Long Range Heliostat Target.

Measurement	Ray Trace	LRHT	Median Error
Peak Flux	1296 W/m^2	1325 W/m^2	.02
Total Power	38160 W	33759 W	.08
95% Beam Width	8.0 m	7.5 m	.06
95% Beam Height	5.9 m	4.3 m	.27
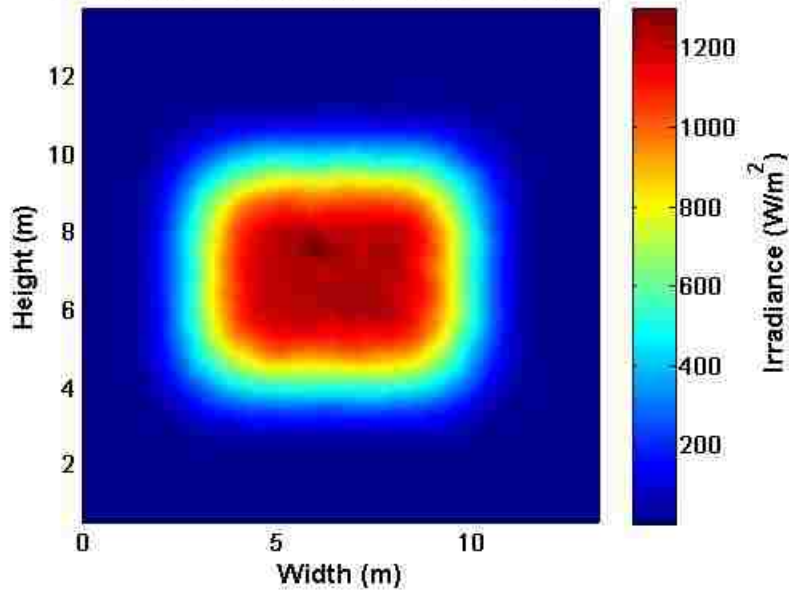
Figure 24. Simulated irradiance distribution on the long-range heliostat target at 1:11pm, July 19, 2012, DNI = 910 W/m^2, RMS slope error = 1 mrad, reflectivity = 0.85, focal length = 1500 m. Peak flux=1,296W/m^2. (Sment, Ho, et al., Flux Characterization System for Long Distance Heliostats 2013)
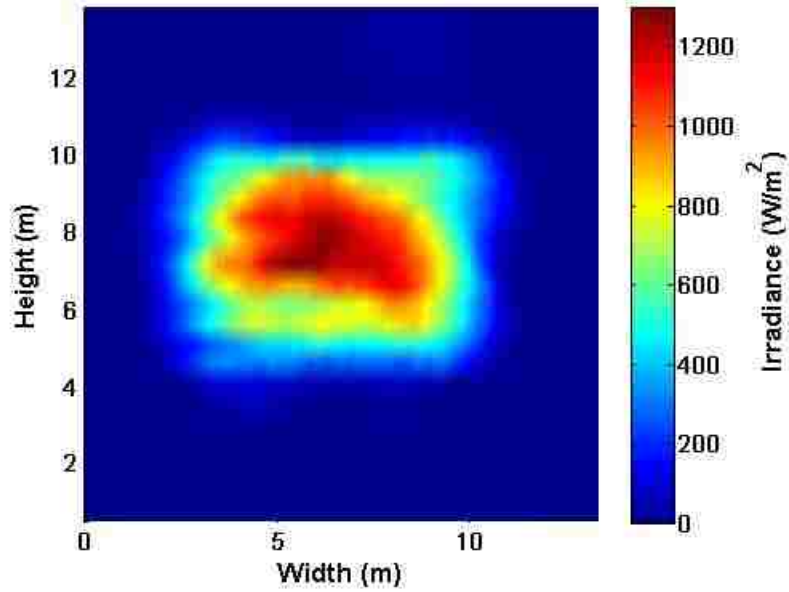
Figure 25: Flux map of test heliostat beam as rendered by LRHT on July 19, 2012 at 1:11pm.

DNI=910, peak flux = 1325 W/m2. (Sment, Ho, et al., Flux Characterization for Long-Distance

Heliostats 2012)

6. APPLICATIONS

The LRHT was used to compare the flux, power, and beam image of a single $1m^2$ facet at 1.7 km, and to detect canting error and improve canting on a previously canted heliostat

6.1 Comparison of Reflective material at Long-Distance

Individual facets were positioned 512 m and 1733 m from the target and mounted on a single-facet rig. The single-facet rig employed a hand powered turnbuckle as an azimuth drive and therefore had variability in the sweep rate (Figure 26). In order to estimate the rig's sweep rate, five timed trials were performed where the technician swept the facet a known angle. The average sweep rate of 4.7 mrad/s was used. The standard deviation was about .26 mrad/s. The distances to the 512 m and 1733 m tests were estimated using Google maps as shown in Figure 27 (right). Figure 27 (left) shows one of the facets as seen from the LRHT located 1733m (1.1 miles) away. (The beam in the figure is not pointed directly at camera.)

Figure 26: Single facet rig. Operator is holding the turnbuckle used as an azimuth drive.

Figure 27: Left: Facet as seek from the portable target at a distance of 1733 m. Right: Map image of facet locations with lines drawn to target. © Google 2012.

The peak flux values measured by the pyranometers have up to 8% error from the LICOR pyranometers plus 2% error from the aiming process plus .78% calibration error. The background irradiance entering the collimated sensor was on the order of 2 W/m^2 and was subtracted from the flux measurements. A generalized error of 10% was applied to stated flux values. The pyranometer heights were measured from the deck of the trailer and are accurate to 1.25 cm. The plotted height on the y-axis may be cropped if the beam exceeded the height of the tower.

6.1.1 Results from Long-Distance Comparison of Reflective Material

While the light from this beam was not detectable on the central receiver tower, the LRHT was able to provide information on the relative performance of two different facets at distances often attained by the extremities of large scale heliostat fields.

Figure 28Figure 29 show the 512 m flux maps of the glass and thin-film facets respectively.   There are similar dimensions and peak fluxes indicating both reflective

materials have a peak flux of about 8/10 suns, have similar dimensions and can deliver similar levels of power.

Flux Map at 512m, Glass: 27-Jul-2012 13:46:34
Peak Flux = 77.3 W/m^2 DNI = 931 W/m^2
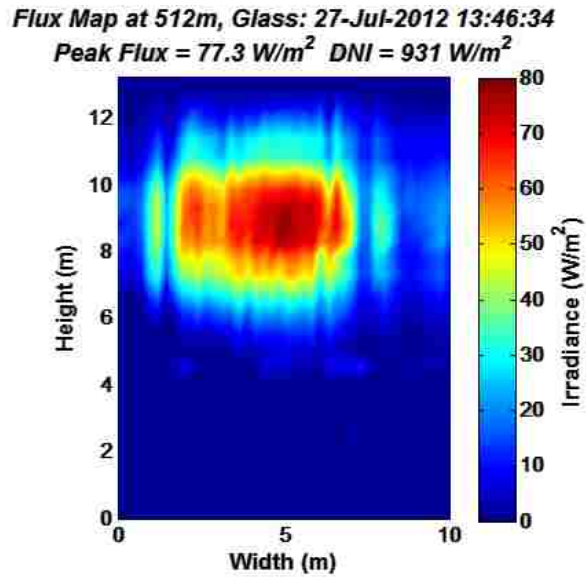
Figure 28: Flux map of single glass facet at 512 m as rendered by LRHT on July 19, 2012 at 1:11pm. DNI=931, peak flux = 77.3 W/m2. (Sment, Ho, et al., Flux Characterization for Long-Distance Heliostats 2012)

Flux Map at 512m, Film: 27-Jul-2012 13:56:34
Peak Flux = 80.8 W/m^2 DNI = 937 W/m^2
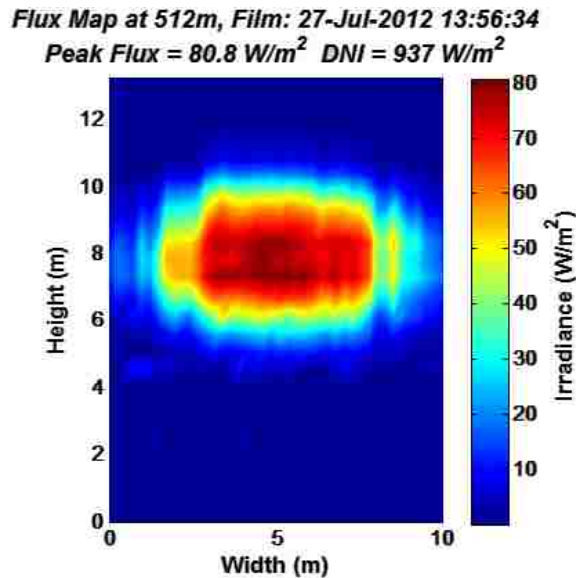
Figure 29: Flux map of single thin film facet at 512 m as rendered by LRHT on July 19, 2012 at 1:11pm. DNI=937, peak flux = 80.8 W/m2. (Sment, Ho, et al., Flux Characterization for Long-Distance Heliostats 2012)

The peak flux measurements of the facets at 1733 are near 1/100th of a sun. Figure 31 summarizes the relative performance of the two facets at 512 m and 1733 m normalized to DNI at the time of sweep. The similar beam size and flux levels indicate the two materials can deliver similar levels of power. Beam image details are not well rendered at this distance but information on the flux and basic size of the beam, particularly the y-axis, may help predict performance of a long-distance heliostat before it is installed.
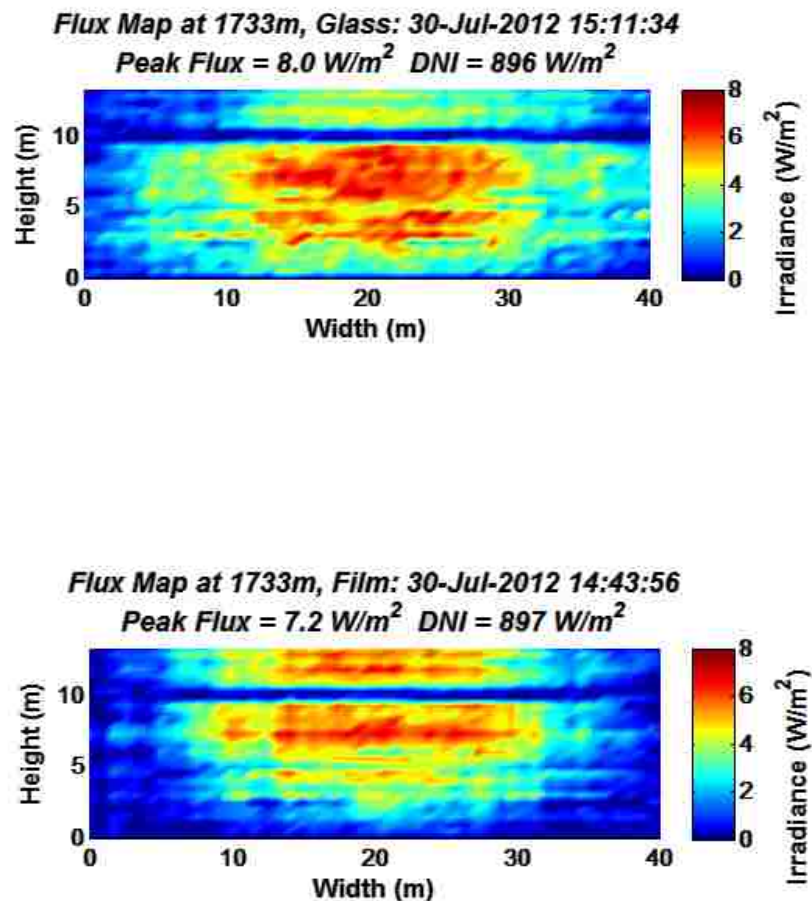
Figure 30: LRHT flux maps of two single facets made of glass (above) and reflective film (below) at a distance of 1733 m. (Sment, Ho, et al., Flux Characterization for Long-Distance Heliostats 2012)
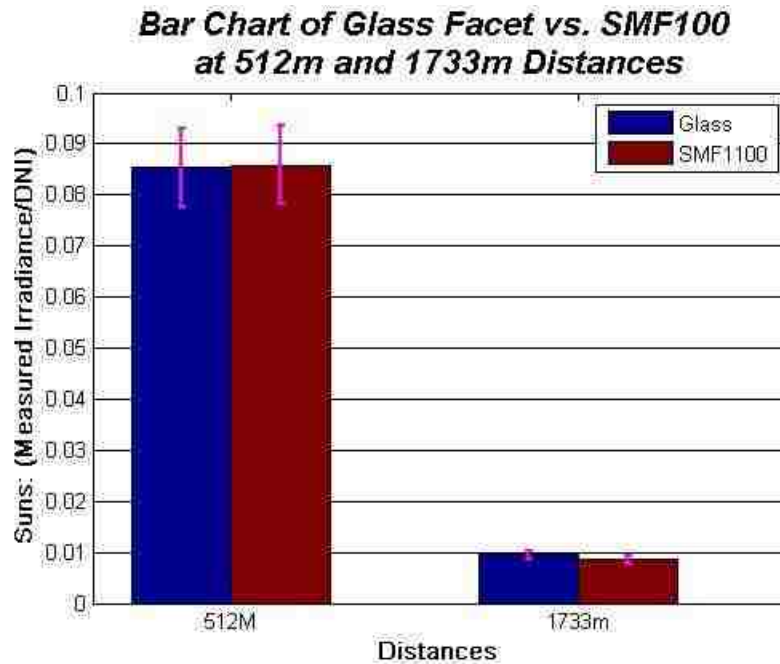
Figure 31: Bar graphs of flux from glass and thin film facets normalized to DNI at time of sweep at 512 m and 1733 m. 10% error bars are shown in pink. (Ho, et al. 2012)

6.2 Canting of Heliostat Using LRHT Flux-Map

In order to improve performance of a heliostat the planes of the several facets that make up a heliostat surface are not perfectly parallel but are slightly rotated and/or tilted in a way that helps the multiple beams from each facet converge on a focal point. The process of rotating or tilting these facets is called canting. A procedure was set up to determine whether the LRHT at any arbitrary location could be used to optimize a heliostat's canting for a certain date on the central receiver. This method could be useful when the central receiver is absent, being prioritized for power production, or when a faster and more precise method such as the Heliostat Facet Alignment and Canting Technique (HFACET) cannot be used.

41

First, a model was created that had perfect canting and focus at the location of the central receiver tower at solar noon on the test date. Then the model was modified to point at the location of the LRHT. The model ray trace of the beam at the LRHT in Figure 32 incorporates canting, focusing, and gravitational deformation of the NSTTF 11E14 heliostat.
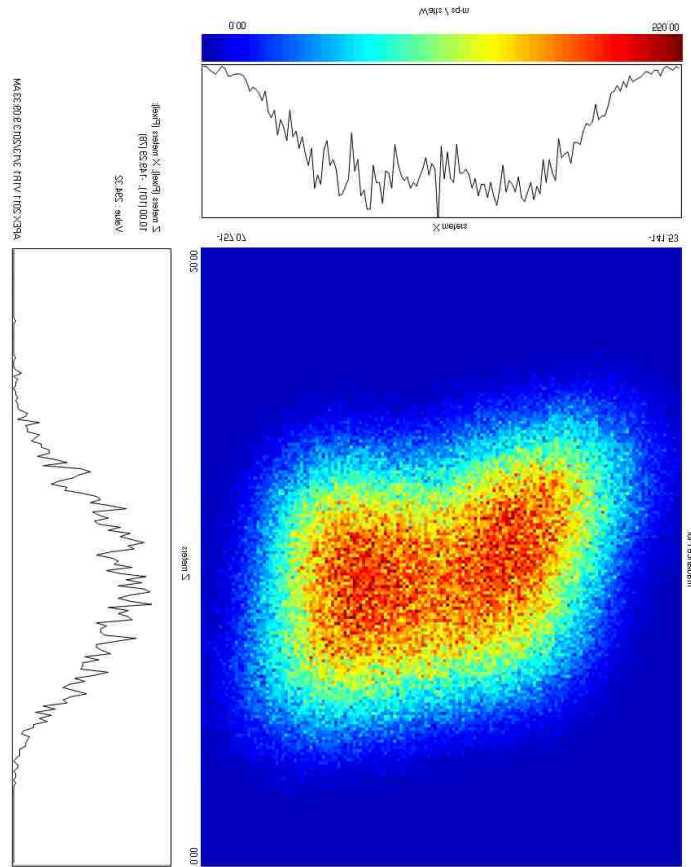
Figure 32: Ray trace of heliostat 11E14 as if it were perfectly canted to the central receiver tower as it would appear at the arbitrary location of the LRHT 436m away. The image shows the bulk of the intensity lying within a 13m wide by 12m high area. The beam also appears to have a butterfly effect where the flux is separable into two centroids due to gravitational sag. Ray trace model courtesy of Joshua Christian.

A flux map was produced on the LRHT and compared to the ideal ray trace. The LRHT was inspected for hot and cool spots, beam spread, and shape. Arrows were drawn

on the flux map to estimate the distance a beam in a hot region must translate in order to fill an adjacent cool region. A metric grid has been overlaid in Figure 33 to estimate the distance the beam from a given facet should move to spread the flux into the cool zones and reform the flux distribution to better match Figure 32 above. For example, Figure 33 shows a very low intensity region in the bottom-right corner near x, y coordinate [8, 4] with an overly intense region (letters C and F) just above it. Neglecting image reversal, this indicates that flux from the facets in the bottom right corner is being aimed too much into the center and they should be rotated downward. Specifically, the lower-right facet(s) is likely pointed at F and should be rotated about the horizontal axis such that the beam points about 2 meters lower.
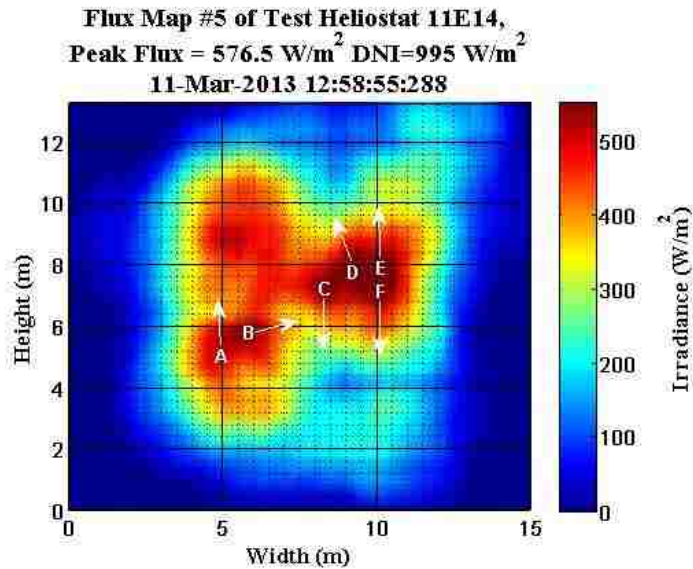
Figure 33: Flux Map. Comparison to the ideal image reveals undesirable hot and cool spots. The arrows indicate the adjustments that were made to distribute the hot spots into the cool areas and make a smoother distribution. The grid is in divisions of meters which were converted to facet angles and eventually screw turns that a technician could use to quickly make the adjustments.

To illustrate the process, an overlay of the inverted heliostat image is shown in Figure 34 with facets numbered F1-F25. Returning to the problematic point F, it can be guessed that the excess flux is probably coming from facets F1 and F6. To create an even distribution, F1 would need to come down about 2 meters to fill in the cold corner region while F6 would need to come down 1 meter to get out of the hot zone but not so far as to create a hot spot in the bottom corner. Once the translation distance of flux at each point was known, the distance was converted to facet angles and ultimately to bolt turns on the canting mechanisms of each facet.

Figure 34: Overlay of mirrored heliostat image and flux map. The arrows illustrate the thought process of determining which facets should be adjusted to move the irradiance to desired regions. The facets are numbered 1:25.

6.2.1 Canting Results

Figure 35 shows the LRHT flux map from the same 11E14 heliostat after two attempts of canting adjustments. The bulk of the flux with intensity above 200 W/m^2 is within a 10m high by 12m wide area which is 16% shorter and 7% narrower than the 12m high and 13m wide region predicted by the ray trace. The hot spots have been redistributed to provide a more even distribution of flux within the central region. The inner region contains two centroids separated by a dividing region sloping slightly to the right. The BCS image in Figure 37 taken of the newly canted 11E14 shows a relatively well-contained and circular beam with a semi-circular centroid a little over 0.6m (2 ft) in diameter.
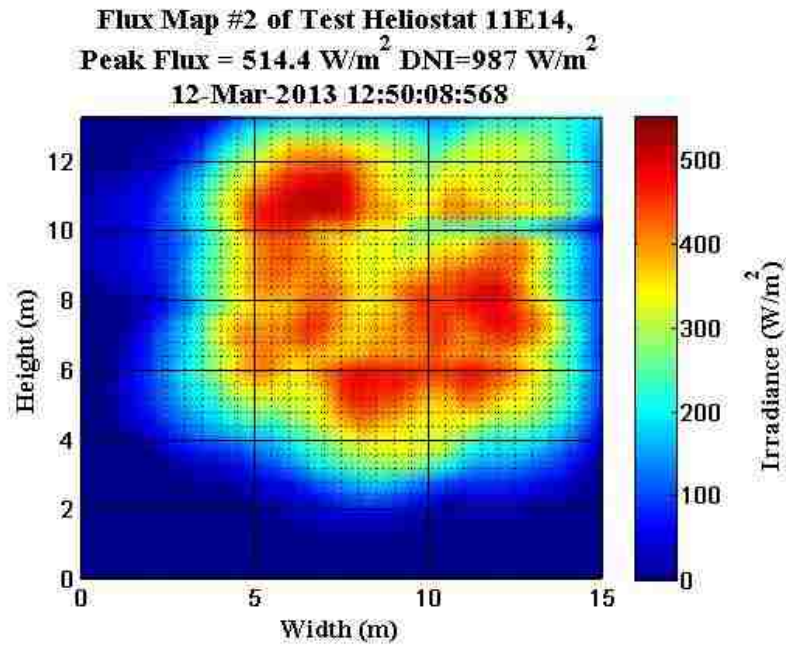
Figure 35: Same NSTTF heliostat 11E14 after canting adjustments. While this image does not approach the ideal distribution, peak flux has dropped precipitously indicating there is less overlap from multiple facets, and there do not appear to be as many hot spots. The image is closer to the preferred square shape. (The unexpected cool patch at [10, 10] is due to a sensor suddenly failing mid-sweep.)
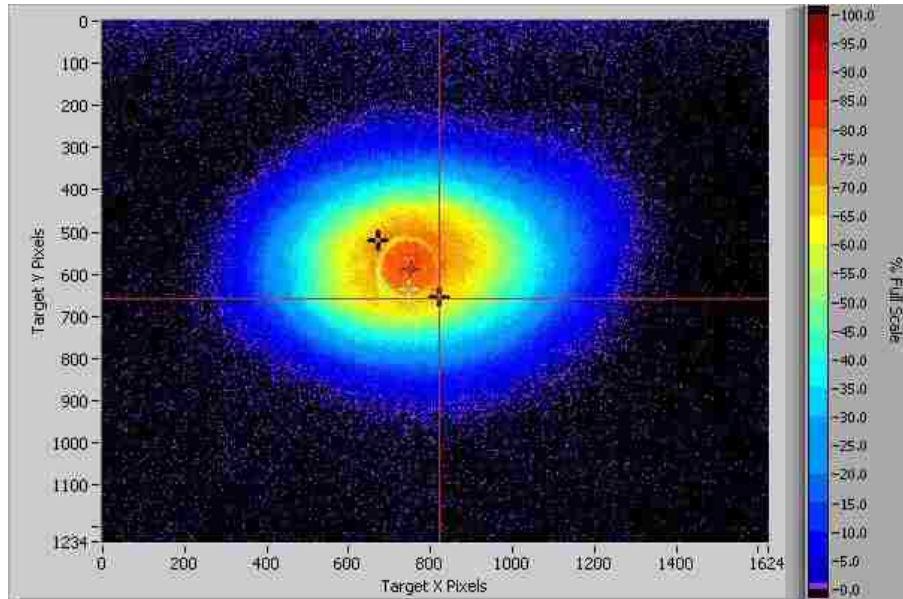
Figure 36: BCS Image of 11E14 previously canted with HFACET taken on Feb. 12, 2013 at 12:49, 28 minutes past solar noon. This is how the beam would have looked before the LRHT canting was performed. The crosses (+) in the plot show a distance of .6 m and can be used to scale the rest of the image.
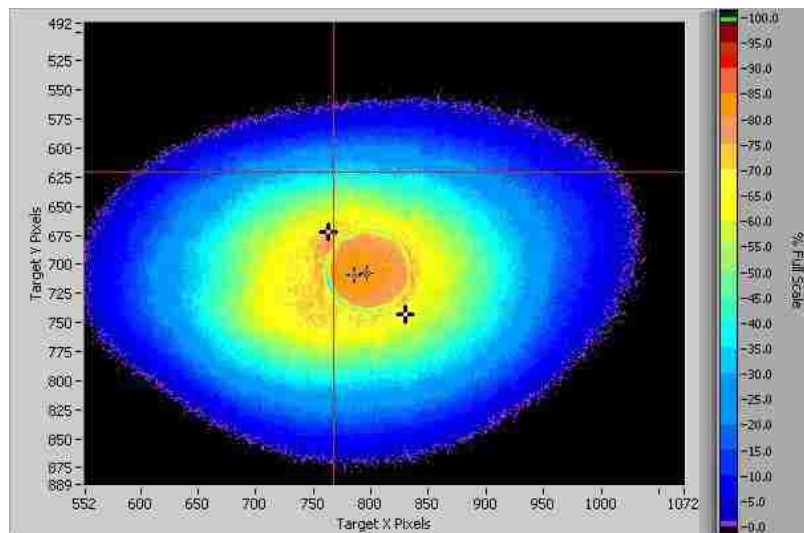
Figure 37: BCS image on central receiver tower after LRHT canting method was performed at 8 minutes past solar noon (March 12, 2013). The canting procedure used on the LRHT at an arbitrary position has produced a relatively well-formed beam at the desired target. The crosses (+) in the plot show a distance of .6 m and can be used to scale the rest of the image.

7. CONCLUSIONS

7.1 Structural Design

The wind loading analysis of the structural redesign shows that the LRHT is very durable and will hold up to any likely wind event. A 38m/s (85mph) gust was recorded at the NSTTF and the tower showed no sign of stress. All components except the anchor bracket which enables the guy wires to connect to the anchor blocks are "off the shelf." In a less regulated environment with no restrictions on using ground anchors, the LRHT system without the concrete blocks weighs less than 181 kg (400 lb) and is more portable. The system that can be assembled from components found anywhere in the world and quickly erected to perform tests on reflectors at any accessible location. The tower would be particularly useful in circumstances where there is a need to test heliostats before the central receiver tower has been built.

The downside of the design is that it is expensive to operate. Since the collimated sensors only allow a 5 degree angle of acceptance and attenuates the signal about 20% for each degree off-axis the sensor is pointed, they must be custom aimed at each target. The operation of this tool either requires a technician to adjust each sensor by hand, or to implement expensive MEMS actuators. While the aiming tool and two-axis mounting brackets allow a sensor to be mounted and aimed in about 2 minutes, targets with several sensors would have a significant delay between sweeps by multiple sources. The actuators may become economical if the tool needed to consistently operate on several sources.

7.2 Collimated Pyranometer Performance in Heliostat Applications

Collimated Pyranometers cost about 20% of a normal incidence pyrheliometer after accounting for materials and assembly labor. Pyranometers also have a nearly instantaneous response that is necessary to capture enough of the beam as it passes in less than 3 seconds. The calibration procedure involves an adjustment for air mass, temperature, angle of incidence, and a calibration constant in order to adapt the response of the pyranometer to the spectral changes in sunlight throughout the day. In the above tests, the angle of incidence modifier was not accounted for due to the careful attempt to make sure there was no angle of incidence between the sensor and the reflector. The air mass function uses coefficients that should be calculated empirically by fitting the response curve to the actual spectral intensity curve. In these tests, the coefficients derived from solar DNI were adopted from the King paper without scrutiny. It is unknown to what extent this adoption has compromised the final values. The calibration constants were acquired by fitting each collimated pyranometer's response to that of an Eppley NIP from one hour before to one hour after air mass 1.5. These coefficients worked well for the first sensors that were used in the evaluation tests and the single facet tests. However, when the tower was moved and the sensors were replaced with new sensors, the images were streaked from incorrect values. The best explanation is that there were certain sensors that were not calibrated properly and in an interpolated plot the few bad sensors cause a lot of bad imagery. The constants would typically adjust the output of each sensor +/- 5% and had a margin of error of about 1.5%. However, there were a few constants that adjusted the reading by up to 14%. It would be advisable in

48

future calibration procedures to double check any sensor that must be changed more than 10% by the calibration constant for procedural error or sensor malfunction.

There are spectral issues to consider when using a pyranometer on reflected light as the sensors are calibrated to operate on atmospheric light while reflected light has certain omitted spectra. A 410 Solar reflectometer was used to measure the spectral reflectance of the sources in most tests above. There does not appear to be any significant dip in any of the bands specified. While spectral error due to absorptivity of the mirrors is likely minimal, there may be air mass issues related to the distance the reflected light has to travel. Adding an additional 1.7 km from the reflector to the target may make the absolute air mass of Albuquerque behave as if it were near sea level.

7.3 Long Range Heliostat Target Validation

The beam shapes produced by the LRHT are difficult to validate without having an actual beam image in the same location to compare to. Some of the images are a little wider or narrower and it is difficult to definitively separate problems related to the LRHT technology from problems with the canting or slope error.

It is also difficult to determine where exactly the boundaries of the beam shape should be. A common method of describing a beam size is to determine the size of the circular or square area in which 95% of the power was contained. In this application the specific geometric dimensions are not as important as determining whether or not the beam will fit on the target. In this application it was necessary to determine whether the height, width, and slant of the beam were reasonably close to the ideal image while accounting

for the idiosyncrasies caused by physical deformations. For this reason it seemed useful to use the 95% method in each dimension rather than a radial or square size per se.

The peak flux measurement was comparable to that produced by a ray trace. This is an encouraging but problematic comparison. While the collimated pyranometers were calibrated to match the Eppley NIP before they were installed on the target, little is known about the effects of reflected light vs. direct solar irradiance on the pyranometers' response. A more definitive procedure could be to install a broadband NIP very near the pyranometers and perform a sweep.

7.4 Comparison of Reflector Performance

The LRHT was able to capture data from single $1m^2$ facets at one mile away. Consistent with other tests performed, the LRHT showed very close comparisons between the reflective film and the glass facets. The combined noise and diffuse light band of the sensors amount to about 2 W/m^2. The peak flux from the facets at 1733 m was about 9.2 W/m^2. The generalized error from the sources itemized in section 3.4.2 is about 10% making these measurements dubiously close to the threshold of uncertainty and thus establishing the outer limit for the LRHT as a 1 m^2 reflector at just over 1.7 km. During a test that is not included above, an attempt was made to test a smaller reflector at the same location and no measurement could be detected.

7.5 Canting with LRHT

The LRHT has demonstrated an ability to be used as a canting tool on a previously canted heliostat. The LRHT may be particularly useful when heliostats cannot be canted

on the central receiver tower due to power production priorities, unexpected construction schedules that may install the heliostats before the tower, or when a faster and more precise method such as the Heliostat Focusing and Canting Technique (HFACET) cannot be used (Sproul, Chavez and Yellowhair 2011).

The problem with canting using the LRHT is that it is computationally and labor intensive. Once the cost of entering the heliostat in CAD, creating an FEA procedure for gravitational deformation, and producing the ray trace has been done for one heliostat, much of the process can be shared with all the other identical heliostats. However, there is still a lot of individualization that must occur as each heliostat is in different relative position to the target and to the sun. Once the new parameters have been entered the FEA can take several hours to solve. Repeating this process on 10,000 heliostats would be ill-advised but if the objective is to evaluate individual heliostats or small batches of heliostats in close proximity this procedure is not overly cumbersome.

It is necessary for the LRHT beam sweep to be performed within several minutes of the modeled ray trace to be sure that the difference in beam shape is not caused by drifting solar position throughout the day. By contrast, the canting process is very quick. A beam sweep of the LRHT only takes a few seconds and the results can be relayed to a technician who can modify the canting, in the case of an NSTTF heliostat design, with a few turns of a bolt. During the evaluation performed above, the technician was able to make an initial adjustment just before the time of the ray trace, see the results, and make a second round of adjustments in time for a second sweep just after the time of the ray trace.

The heliostat used in the test was slightly problematic and not producing an ideal image but it had been previously canted using the HFACET technology. More testing on previously uncanted heliostats would be needed to determine the limits on initial heliostat conditions for which this "proximity method," used to inform an educated guess on the facet adjustments, could be used. The method is best suited for previously canted heliostats and may not be valid in circumstances where the hot spots are caused by facets from other areas of the heliostat.

8. RECOMMENDATION OF FUTURE WORK

The scope of this initial test was to design build and validate a portable heliostat target. The promising results present good potential for future work in the arena of long-distance flux mapping.

8.1 Tracking Error Analysis

It may be possible to determine the tracking error with the LRHT. The beam could be swept a few times to establish a learning or training flux map. The heliostat could then be programed to track on the center of the target. The position of the beam could then be determined using statistical similarity between the new reading by the sensors and the previous array of readings. The distance between the most similar flux reading and the beam centroid would equal the tracking error.

Tracking error detection would also be well-suited for an artificial neural network. A radial bias network would provide centers based on data points chosen randomly or in a 1x1 meter matrix with a certain diameter based on standard deviation that encompasses a specified amount of variability around the grid point. When the beam is set to track on the tower, the new input would be compared to the original training sweep data and by a gradient descent algorithm, the network could converge on which radial center was most similar to the particular transect and hence classifying the position of the beam on the tower.

Figure 38 shows sensor intensity readings over time as a heliostat was centered on the target and manually adjusted periodically. The parallel or divergent gradients indicate how the beam is moving horizontally or vertically over the peak intensity regions. In

circle 1 of Figure 38, the parallel slopes indicate a horizontal motion toward a hotter region. In circle 2, crossing motion of the gradients show a vertical adjustment as a given area of the beam moves from one sensor to the next. Circle 3 shows that the peak flux is located in sensor 18 which is slightly above the midpoint of the beam. If a relationship between the mutual peak intensity area and centroid can be determined, this method could be developed as a means of finding the centroid.
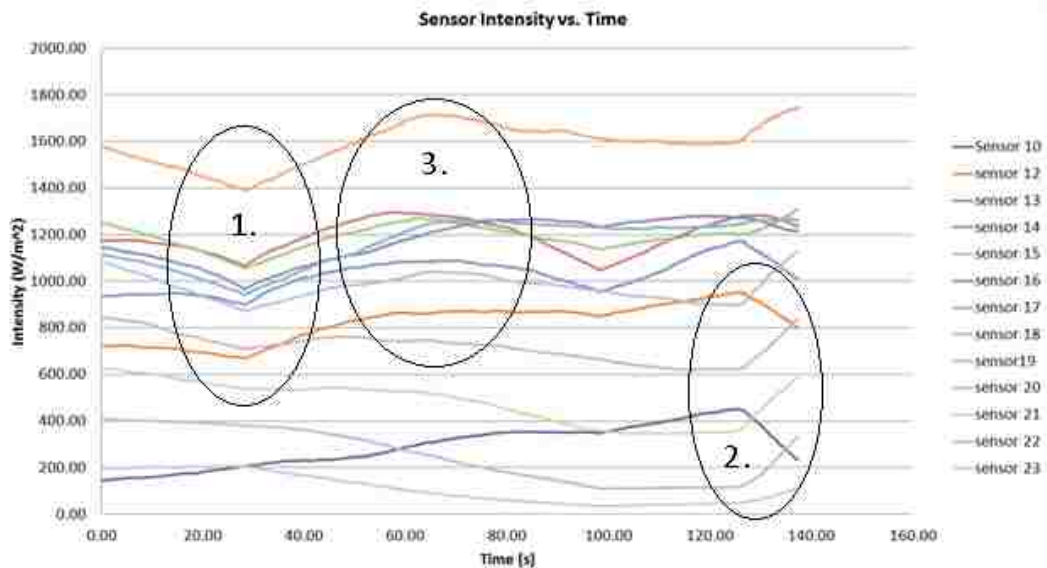
Figure 38. Sensor intensity over time. The beam is contained within the height of sensors 10-23. The sensor with the greatest intensity is sensor 18. 1. Parallel motion in intensity occurs as the beam is adjusted horizontally and all sensors move toward or away from the centroid. 2. Crossed intensity indicates vertical motion of the heliostats as sensors begin to swap intensity bands.

8.2 Alternative Aiming Procedures

One of the set-backs to the current design is that all the sensors have to be adjusted by hand to aim at each new target location. At greater initial material cost and subsequent

labor cost savings, the tower could be housed in a bearing such that the triangular truss is mounted into a circular adaptor connected to a bearing which is connected on the outside to the guy wires. In this sense, the tower could be set up for a given focal distance and height such as 1 km or 0.5 km at 3 meters and then the target could rotate instead of the reflector surface. This is useful for testing multiple heliostats in radial formations. Ultimately, electro-mechanical actuators could be utilized to provide rapid focusing optimized to any location.

9. SUMMARY

The LRHT has shown an ability to quickly characterize heliostats and facets at long distances. While the characterizations are qualitatively promising, efforts to quantify the accuracy of the flux maps are somewhat problematic due to an inability to model the real-world imperfections and deformations in the heliostat as it moves the beam from the BCS target to the portable target. Results show agreement between the flux measurements of these sensors and modeled ray tracing to be within 5%. Beam dimensions and centroidal abnormalities show qualitative similarities to those rendered by ray trace models and BCS photos taken on the nearby central receiver tower.

The target is portable and can be driven via flatbed trailer to a test site and quickly assembled. Analysis of wind loading shows that the tower is safe and will not fail during a 45m/s wind. The low-cost LI-200 pyranometers are collimated and calibrated to behave similarly to more expensive Eppley pyrheliometers.

A heliostat was tested at a distance of ~340 m and two single facets were tested at ~500 and ~1700 m. Flux values were logged as the beams were swept horizontally across the column of sensors at an even rate yielding an irradiance distribution along discrete vertical transects corresponding to the heights of the sensors. Interpolation was then used to render the entire irradiance distribution into a flux map. The peak flux and estimated height and width of the interpolated beam image were compared to the results of a beam analysis modeled by ray tracing. Qualitative features in the beam images rendered by the LRHT were compared to images taken on the nearby central receiver tower and show many similarities.

In the case of the single facets at 1700 m, while the beam image was not detectable on the face of the central receiver tower, the long-range heliostat target was able to measure the flux and provide a fuzzy but informative beam image with an estimate of peak flux and beam spread.

An LRHT flux map was compared to a modeled beam image canted to the central receiver tower but located at the arbitrary distance of the LRHT. Adjustments were made to evenly distribute the flux from hot regions to cool regions and shape the beam like the modeled image. The resulting beam on the central receiver tower appeared to be well formed although no quantitative criteria was established to compare the beam to its previous form.

APPENDIX A. WIND SURFACE AREA CALCULATIONS

Aluma provided an effective wind surface area on the tower of 2.7 m^2 (4320 in^2). (Kidd 2011) Local wind forces were based on a total measured wind surface area of 3.6 m^2 (5637 in^2) which is 30% larger and hence, more conservative. The cosine loss of surface area on truss members presented at an angle to the oncoming wind was factored. The wind blockage on vertical members was factored in the surface area estimate. Neither blockage from horizontal and diagonal truss members on each other nor on the mast was subtracted in the calculation below. This accounts for much of the discrepancy in surface area values.
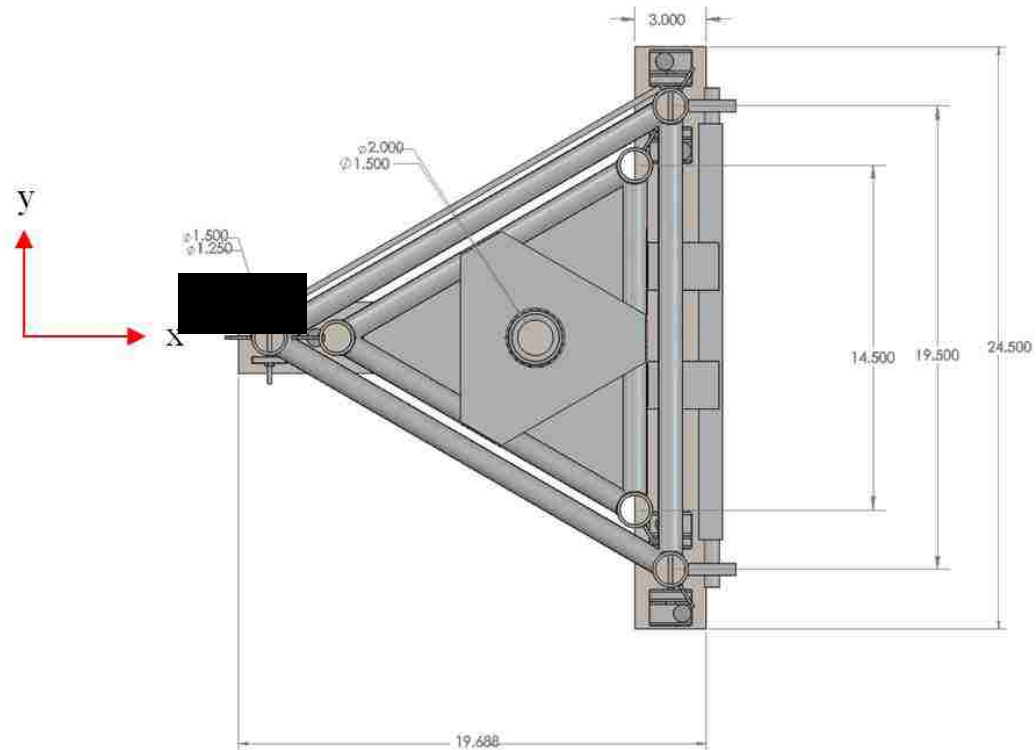
Figure 39: Top view tower dimensions in inches. (metric diagram unavailable)

58

Table 6: Nomenclature tower dimensions

Table of Nomenclature
$l_v = 7.6$ m (300 in) = length of vertical members
$t_v = 3.1$ cm (1.25 in) = thickness of vertical members
$l_{lh} = 46$ cm (18.25 in) = length of lower horizontal member
$l_{ld} = 66$ cm (26 in) = length of lower diagonal member
$l_{uh} = 34$ cm (13.25 in) = length of upper horizontal member
$l_{ud} = 58$ cm (22.75 in) = length of upper diagonal member
$t_{hd} = 2.5$ cm (1 in) = thickness of horizontal and diagonal member
$M_l = 2.4$ m (96 in) = length of Mast
$M_t = 5.1$ cm (2 in) = thickness of Mast
$S_l = 23$ cm (9 in) = length of senor housing
$S_w = 3.8$ cm (1.5 in) = width of sensor housing
$N_v = 3$ = number of vertical members per truss
$N_{lh} = 17$ = number of lower horizontal rungs
$N_{ld} = 13$ = number of lower diagonal members
$N_{uh} = 17$ = number of upper horizontal members
$N_{ud} = 7$ = number of upper diagonal members
$N_s = 35$ = number of sensors
$A_m = M_l M_t = 0.124$ m^2 (192 in^2) = mast area
$A_s = S_l S_w = 0.0087$ m^2 (13.5 in^2) = sensor area
$A_a = A_h A_w = 0.557$ m^2 (864 in^2) = anchor area

Area of lower truss

$$A_l = N_v(l_v t_v) - (N_{lh} + N_{ld})(t_v) +$$

$$(N_{lh}(l_{lh}t_{hd}) + N_{ld}(l_{ld}t_{hd}))\big(1$$

$$+ 2\cos(30°)\big) = 1.82 \text{ m}^2 \ (2828 \text{ in}^2)$$

(3.2.)

Area of upper truss

$$A\_u = N\_v \, (l\_v \, t\_v) - (N\_lh + N\_ld)(t\_v)$$
$$+ N\_uh \, (l\_lh \, t\_hd \, ")$$
$$+ " \, N\_ud \, "(" \, l\_ud \, t\_hd \, ")$$
$$= 1.38 \ \text{m}^2 \ (2145 \ \text{in}^2)$$

(3.3.)

Total Tower Area

$$A_{tot} = A_l + A_u + A_m + NA_s = 3.7 \ \text{m}^2 \ (5734 \ \text{in}^2)$$

(3.4.)

APPENDIX B. CFD PRESSURE ANALYSIS

SolidWorks Flow Simulation was used to analyze the pressures formed in a 101 kPa and 44 m/s boundary condition wind aimed directly normal to the vertical plane of the tower (Figure 40). The mesh used 1.5 million total cells including 500 thousand partial surface/fluid cells.
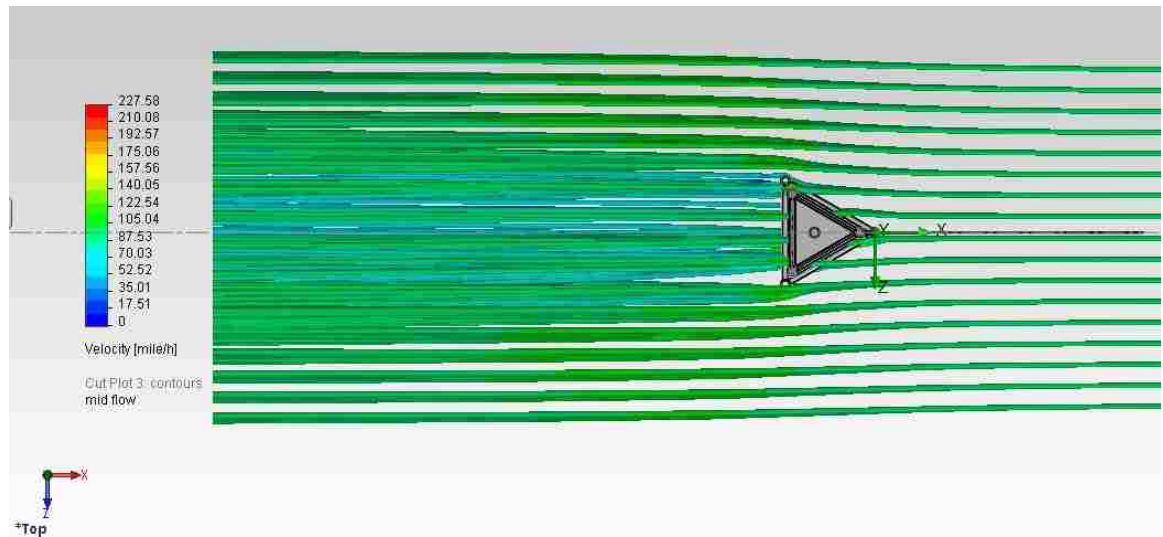
Figure 40: Flow Trajectories around tower from right to left. Velocities are in miles per hour.
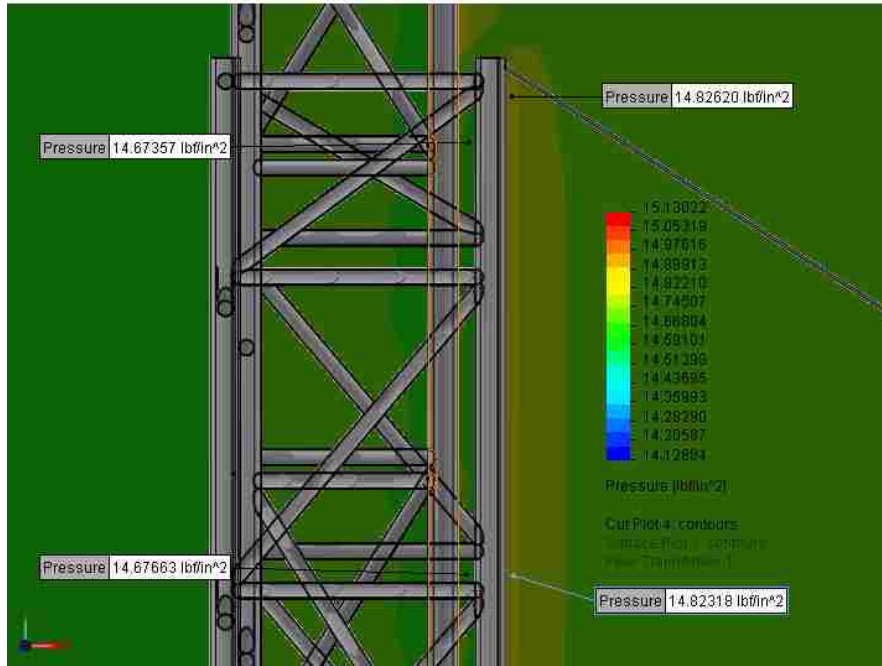
Figure 41: CFD model, close up of pressure field around truss under 45 m/s winds. There is an average differential between the windward and leeward side of the beam of 0.2 psi or 1.3 kPa. With a 3.6 m² area an average total force of 4.7 kN (1052 lb) would be transferred to guy wires.

Table 7: Nomenclature for CFD results

Table of CFD Results
$\Delta P = \mathbf{1.3\ kPa}\ (\mathbf{0.2}\ \text{psi}) = $ average pressure difference accross a member
$F_{lC} = \Delta P A_{l\text{(in)}} = 2518\ \text{N}\ (566\ \text{lb}) = $ Wind force on lower truss
$F_{uC} = \Delta P A_{u\text{(in)}} = 1908\ \text{N}\ (429\ \text{lb}) = $ Wind force on upper truss
$F_{mC} = \Delta P A_{m\text{(in)}} = 169\ \text{N}\ (38\ \text{lb}) = $ Wind force on mast
$F_{sC} = \Delta P N A_{s\text{(in)}} = 420\ \text{N}\ (94.5\ \text{lb}) = $ Wind force on sensors

APPENDIX C. SIMPLIFIED DRAG FORCE
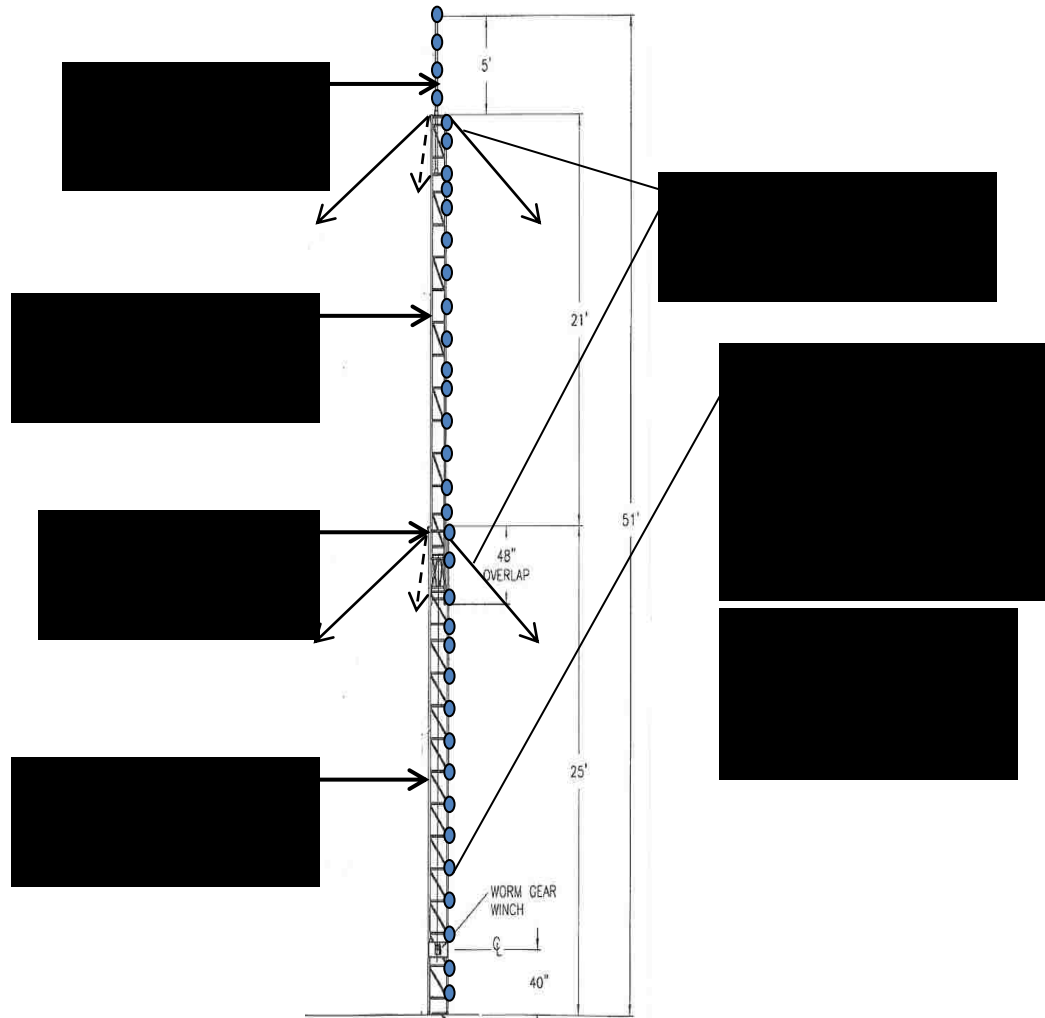
Figure 42: Sensor Layout and summary of forces acting on Aluma Tower T-50XHD tower in 45 m/s (100 mph) wind.

Table 8: Nomenclature for simplified drag force calculation

Table of Nomenclature
$U = 45$ m/s $(146\ \text{ft}/\text{s})$ = **target wind speed**
$D = 0.307$ cm (0.104 ft) = diameter of large tower pipe
$\nu = 18.9\ \text{m}^2/\text{s}\ (0.000158\ \text{ft}^2/\text{s})$ = **kinematic viscosity**
$Re = \dfrac{UD}{\nu} = 96,101$ = **Reynolds number**
$C_d = 1.2$ = Drag Coefficient for circular tube
$\rho = 1.18\ \text{kg}/\text{m}^3 = 0.00256\ \text{slug}/\text{ft}^3$ = density of air at 25° C

Wind force on lower truss	$F_l = \dfrac{1}{2} C_d \rho U^2 A_{l(\text{ft})} = 2856$ N (642 lb)	(3.5.)
Wind force on upper truss	$F_u = \dfrac{1}{2} C_d \rho U^2 A_{u(\text{ft})} = 2171$ N (488 lb)	(3.6.)
Wind force on mast	$F_m = \dfrac{1}{2} C_d \rho U^2 A_{m(\text{ft})} = 196$ N (44 lb)	(3.7.)
Wind force on sensors	$F_s = \dfrac{1}{2} C_d \rho U^2 N A_{s(\text{ft})} = 476$ N (107 lb)	(3.8.)
Total Wind Force on Tower	$F_s = \dfrac{1}{2} C_d \rho U^2 N A_{s(\text{ft})} = 5698$ N (1281 lb)	(3.9.)

64

APPENDIX D. TIA-22-G STANDARD

Table 9: Nomenclature for Standard TIA-22-G (Kidd 2011)

Table of Nomenclature
$z = 15.5$ m (51 ft) = height above ground
$z_g = 1619$ m (5312 ft) = elevation
$a = 7$ = constant
$K_z = 2.01\left(\dfrac{z}{z_g}\right)^{2/a} = .532$ = velocity pressure coefficient
$K_{zmin} = .7$ = alternative minimum velocity pressure coefficient
$K_{zt} = 1$ = topographic category
$K_d = .85$, for lattices structures with triangular cross sections
$I = .87$, constant for class 1 structure

Wind force on lower truss
$$F_{\text{TIA-}l} = \rho K_{zmin} K_d K_{zt} U_{\text{mph}}{}^2 I A_l = 1339 \text{ N (301 lb)} \qquad (3.10.)$$

Wind force on upper truss
$$F_{\text{TIA-}u} = \rho K_{zmin} K_d K_{zt} U_{\text{mph}}{}^2 I A_u = 1014 \text{ N (228 lb)} \qquad (3.11.)$$

Wind force on mast
$$F_{\text{TIA-}m} = \rho K_{zmin} K_d K_{zt} U_{\text{mph}}{}^2 I A_m = 89 \text{ N (20 lb)} \qquad (3.12.)$$

Wind force on sensors
$$F_{\text{TIA-}s} = \rho K_{zmin} K_d K_{zt} U_{\text{mph}}{}^2 I N A_s = 222 \text{ N (50 lb)} \qquad (3.13.)$$

APPENDIX E. GUY WIRE TENSION CALCULATIONS

It was conservatively assumed that the worst case wind event would be aimed directly normal to the vertical tower plane placing all the tension into a single pair of guy wires and a single anchor. It was also assumed that all wind energy transferred to the surface of the truss would be eventually distributed to the nodes at the bolts and the guy wire mounting points. The guy wire tension was modeled to be the simple ratio of forces transmitted to the lower guy wire or the upper guy wire as a matter of proximity. Note the 1.5 kN (341 lbf) of shear force that is transmitted to three 9.5 mm (3/8 in) bolts in the base of the tower will be the only forces transmitted to the baseplate on the trailer.

Figure 43: Guy wire layout: front view and top view. Dimensions are in feet. (Aluma Tower Company, Inc 1997)

Table 10: Nomenclature for tension calculation in guy wires

Table of Nomenclature
$h_t = 15.5$ m (51 ft)=height of tower
$h_{ug} = 14$ m(46 ft)=upper guy wire attachment height
$h_{lg} = 7.6$ m (25 ft)=lower guy wire attachment height
$h_{lm} = 3.8$ m (12.5 ft) =midpoint of lower truss
$h_{um} = 10.8$ m (35.5 ft)=midpoint of upper truss
$h_{mm} = 13.5$ m (44.5 ft)=midpoint of mast
$\theta_l = 32° =$ lower guy wire angle
$\theta_u = 49° =$ upper guy wire angle
$T_{lpx} = 100 \cos(\theta_l) = 377$ N (84.8 lb) = Pre-tension in lower guy wire
$T_{lpy} = 100 \sin(\theta_l) = 236$ N (53 lb) = Pre-tension in lower guy wire
$T_{upx} = 100 \cos(\theta_u) = 294$ N (66 lb) = Pre-tension in lower guy wire
$T_{upy} = 100 \sin(\theta_u) = 334$ N (75 lb) = Pre-tension in lower guy wire

$\hat{x}$ wind tension
in lower guy wire

$$T_{lwx} = \left(F_l + N_{l\hbar}F_{\frac{s}{unit}}\right)\left(\frac{h_{lm}}{h_{lg}}\right) + \tag{3.14.}$$

$$\left(F_u + 14F_{\frac{s}{unit}}\right)\left(\frac{(h_{ug} - h_{lg}) - (h_{um} - h_{lg})}{(h_{ug} - h_{lg})}\right) +$$

$$\left(F_m + 4F_{s/unit}\right)\left(\frac{(h_{ug} - h_{lg}) - (h_{mm} - h_{lg})}{(h_{ug} - h_{lg})}\right)$$

$$= 2736 \text{ N (615 lb)}$$

67

$\hat{x}$ wind tension
in upper guy wire

$$T_{uwx} = \left(F_u + 14F_{\frac{s}{unit}}\right)\left(\frac{h_{um} - h_{lg}}{h_{ug} - h_{lg}}\right) + \tag{3.15.}$$

$$(F_m + 4Fs)\left(\frac{(h_{mm} - h_{ug}) - (h_{mm} - h_{lg})}{(h_{ug} - h_{lg})}\right)$$

$$= 930 \text{ N } (209 \text{ lb})$$

$\hat{x}$ shear force
in bolts

$$F_b = \left(F_l + N_{lh}F_{s/unit}\right)\left(\frac{h_{lm} - h_{lm}}{h_{lg}}\right) = 1517 \text{ N } (341 \text{ lb}) \tag{3.16.}$$

$\hat{y}$ wind tension
in lower guy wire

$$T_{lwy} = T_{lwx}\tan(\theta_l) = 3114 \text{ N } (700 \text{ lb}) \tag{3.17.}$$

$\hat{y}$ wind tension
in upper guy wire

$$T_{uwy} = T_{lwx}\tan(\theta_u) = 1068 \text{ N } (240 \text{ lb}) \tag{3.18.}$$

Total tension
in lower guy wire

$$T_l = \sqrt{T_{lwx}^2 + T_{lpx}^2 + T_{lwy}^2 + T_{lpy}^2} \tag{3.19.}$$

$$= 4426 \text{ N } (995 \text{ lb})$$

Total tension
in upper guy wire

$$T_u = \sqrt{T_{uwx}^2 + T_{upx}^2 + T_{uwy}^2 + T_{upy}^2} \tag{3.20.}$$

$$= 1485 \text{ N } (334 \text{ lb})$$

APPENDIX F. CONCRETE ANCHOR FORCES

The summed tension in the guy wires was used as the active forces on the concrete anchors. The x force would need to be balanced by the force of friction on the concrete as a function of normal force. The upward y tension was subtracted from the normal force. The moments were calculated about the 61 cm width dimension in order to view the most vulnerable aspect ratio configuration even though the anchors are positioned such that the 61 cm dimension is height whenever possible.

Table 11: Nomenclature for force and moment calculations on anchor

Table of Nomenclature
$\rho_c = 150 \ ^{\text{lb}}/_{\text{ft}^3}$ = density of concrete
$\mu_c = .35$ = friction coefficient concrete/sand
$w_c = 2$ ft = width of anchor
$h_c = 3$ ft = height of anchor
$l_c = 5$ ft = length of anchor

$\hat{x}$ wind tension in both guy wires plus wind force

$$T_x = T_{lwx} + T_{uwx} + T_{lpx} + T_{upx} + \frac{1}{2}C_d\rho U^2 A_{a(\text{ft})} \tag{3.21.}$$

$$= 1170 \text{ lb}$$

$\hat{y}$ wind tension in both guy wires plus wind force

$$T_y = T_{lwy} + T_{uwy} + T_{lpy} + T_{upy} = 1068 \text{ lb} \tag{3.22.}$$

Minimum weight
required of
concrete

$$W_{min} = \frac{T_x}{\mu_c} + T_y = 4411 \text{ lb}$$

(3.23.)

The moments on the concrete anchor would be the weight of the anchor multiplied by the width resisting the tipping minus the tension in the cables causing the tipping moment. Wind forces on the block would not cause significant moment. Hence the net positive moment below shows the extent to which the concrete anchor will resist tipping.

Net moment
resisting tipping
of concrete anchor

$$W_c \frac{w_c}{2} - T_x h_c - T_y \frac{w_c}{2} = 1510 \text{ lb-ft}$$

(3.24.)

APPENDIX G. TRAILER MOMENTS

The moments upon the trailer include the 2200 lb weight of the trailer times the width minus the shear force in the bolts times the height. The outriggers are omitted as they are only necessary in the event that the tipping force prevails at which point each outrigger will experience approximately a 1/45 fraction of the net force as is shown in equations 3.25 and 3.26.

Table 12: Nomenclature for trailer moment calculations

Table of Nomenclature
$W_t = 2200$ lb=curb weight of trailer
$w_t = 4.5$ ft = span of trailer drop-leg jacks
$h_t = 3.3$ ft = height of trailer
$l_t = 40$ ft = length of trailer
$l_o = 22.5$ ft = additional length of outriggers

net moment resisting tipping of concrete trailer

$$\frac{W_t}{2}\frac{w_t}{2} - F_b h_t = 1349 \text{ lb-ft} = M_t \tag{3.25.}$$

net force on leeward outriggers

$$\frac{M_t}{l_o} = 60.0 \text{ lb} \tag{3.26.}$$

REFERENCES

Aluma Tower Company, Inc. "2-25CG Guy Kit." *Tower Guying Assembly.* Vero Beach, Fl: Aluma Tower Company, Inc, January 9, 1997.

Aluma Tower Company, Inc. "Technical Manual for Aluma Towers." *Instructions for Installing & Operating a Tower on a Concrete Pad Next to a Building.* Vero Beach, Fl: Aluma Tower Company, Inc, September 18, 1997.

Duffie, John A, and William A. Beckman. *Solar Engineering of Thermal Processes.* 2nd. New York: John Wiley and Sons, Inc, 1991.

Fisher, Dan. *Response Time Comparison of an Eppley Normal Incidence Pyrheliometer (NIP) and a LI-COR LI-200 Pyranometer with Attached Collimator.* Albuquerque, NM: Sandia National Laboratories, 2010.

Griffith, Daniel Todd, Adam C Moya, Clifford K Ho, and Patrick S. Hunter. "Structural Dynamics Testing and Analysis for Design Evaluation and Monitoring of Heliostats." *ESFuelCell2011-54222.* Washington, DC: ASME, 2011.

Ho, Clifford K, Jeremy Sment, James Yuan, and Cianan Sims. "Characterization of Metallized Polymer Films for Long-Distance Heliostat Applications." *SolarPACES 2012.* Marrakech, Morocco: SolarPACES, 2012.

Hosoya, Noriaki, and Jon A Peterka. *Heliostat Wind Load Data Analysis, Interim Report CPP Project 98-1590.* Fort Collins, CO: Cermak Peterka Patersen, Inc, 1998.

Ineichen, Pierre, and Richard Perez. "A New Airmass Independent Formulation of the Linke Turbidity Coefficient." *Solar Energy* (Elsevier Science Ltd) 73 (2002): 151-157.

Kidd, Todd, Mechanical Engineer at Aluma Tower Company, interview by Jeremy Sment. *Direct Inquiry* (August 22, 2011).

King, David L., and Daryl R. Meyers. "Silicon-Photodiode Pyranometers: Operational Characteristics, Historical Experiences, and New Calibration Procedures." *IEEE 26th PVSC Sept. 30-OCt. 3, 1997*. Anaheim, CA: IEEE, 1997. 1285-1288.

King, David L., Jay A. Kratochvil, and William E. Boyson. "Measuring Solar Spectral and Angle-of-Incidence Effects on Photovoltaic Modules and Soalr Irradiance Sensors." *26th PVSC; Sept. 30-Oct. 3, 1997*. Anaheim, CA: IEEE, 1997. 1113-1116.

King, David L., William E. Boyson, and Ward I. Bower. "Improved Accuracy for Low-Cost Solar Irradiance Sensors." *2nd World Conference and Exhibition on Photovoltaic Solar Energy Conversion, 6-10 July 1998.* Vienna, Austria: Sandia National Laboratories, 1998.

Kuntz Falcone, Patricia. *A Handbook for Solar Central Receiver Design.* Livermore, CA: Sandia National Laboratories, 1986.

LI-COR Biosciences. "LI-200SA Pyranometer Sensor Brochure - LI-COR Biosciences." *www.licor.com.* n.d. www.licor.com/env/pdf/light/200.pdf.

—. *LI-COR Terrestrial Radiation Sensors, Instruction Manual.* Lincoln, Ne: LI-COR Inc, 2005.

"Lifting Pin Anchor System." *patterson-online.com.* 09 13, 2011. http://www.patterson-online.com/Products/categories.aspx?CatID=296&MasterCat=N&Parent=209,296 .

Maxwell, Eugene L. *A Quasi-Physical Model for Converting Hourly Global Horizontal to Direct Normal Insolation.* Vols. SERI/TR-215-3087. Golden, CO: Solar Energy Research Institute, 1987.

Perez, R, and P Ineichen. "Modeling daylight availability and irradiance components from direct and global irradiance." (Solar Energy) 44 (1990).

Perez, Richard R, Pierre Ineichen, Eugene L. Maxwell, Robert D. Seals, and Antoine Zelenka. "Dynamic Global-to-Direct Irradiance Conversion Models." *ASHRAE*, 1992: 354-369.

Perez, Richard, and Pierre Ineichen. "A New Operational Model for Satellite-Derived Irradiances: Description and Validation." *Solar Energy* (Elsevier Science Ltd) 73, no. 3 (2002): 307-317.

Perez, Richard, and Pierre Ineichen. "A new simplified version of the Perez Diffuse Irradiance model for tilted surfaces." *Solar Energy*, 1987: 221-231.

Peterka J.A., R.G. Derickson. *Wind Load Design Methods for Ground Based heliostats and Parabolic Dish Collectors.* Fort Collins, Colorado: Colorado Stae University, 1992.

Reda, Ibrahim, and Afshin Andreas. *Solar Position Algorithm for Solar Radiation Applications.* Golden, Colorado: NREL, January 2008.

Sandia, Sterling Energy Systems Sets new world record for solar-to-grid conversion efficiency. February 12, 2008. https://share.sandia.gov/news/resources/releases/2008/solargrid.html (accessed January 18, 2013).

Sment, Jeremy N, Clifford K Ho, Adam C Moya, and Cheryl Ghanbari. "Flux Characterization for Long-Distance Heliostats." *SolarPACES*. Marrakech, Morroco: SolarPACES, 2012.

—. "Flux Characterization System for Long Distance Heliostats." *AS FUEL CELL 2013*. Minneapolis, MN: ASME, 2013.

Speir, Mark, interview by Jeremy Sment. *Direct Inquiry* (December 1, 2012).

Sproul, Evan, Kyle Chavez, and Julius Yellowhair. "Development of Heliostat Focusing and Canting Enhancement Technique: an Optical Heliostat Alignment Tool for the NSTTF." *Proc. ASME ES2011*. Washington, DC: ASME, 2011.

US Department of Energy. *Solar Multimedia.* November 8, 2012. https://www.eeremultimedia.energy.gov/solar/ (accessed December 21, 2012).

Yuan, James, Joshua Christian, and Clifford K Ho. "Compensation of Gravity Induced Heliostat Deflections for Improved Optical Performance." *ASME ES Fuel Cell 2013*. Minneapolis, MN: ASME, 2013.